Modes of Storm-Scale Variability and Tornado Potential in VORTEX2 Near- and Far-Field Tornadic Environments

MATTHEW D. FLOURNOY[a]

School of Meteorology, University of Oklahoma, Norman, Oklahoma

MICHAEL C. CONIGLIO

NOAA/National Severe Storms Laboratory, and School of Meteorology, University of Oklahoma, Norman, Oklahoma

ERIK N. RASMUSSEN

Cooperative Institute for Mesoscale Meteorological Studies, Norman, Oklahoma

JASON C. FURTADO

School of Meteorology, University of Oklahoma, Norman, Oklahoma

BRICE E. COFFER

Department of Marine, Earth, and Atmospheric Sciences, North Carolina State University, Raleigh, North Carolina

(Manuscript received 12 May 2020, in final form 24 July 2020)

ABSTRACT

Some supercellular tornado outbreaks are composed almost entirely of tornadic supercells, while most consist of both tornadic and nontornadic supercells sometimes in close proximity to each other. These differences are related to a balance between larger-scale environmental influences on storm development as well as more chaotic, internal evolution. For example, some environments may be potent enough to support tornadic supercells even if less predictable intrastorm characteristics are suboptimal for tornadogenesis, while less potent environments are supportive of tornadic supercells given optimal intrastorm characteristics. This study addresses the sensitivity of tornadogenesis to both environmental characteristics and storm-scale features using a cloud modeling approach. Two high-resolution ensembles of simulated supercells are produced in the near- and far-field environments observed in the inflow of tornadic supercells during the second Verification of the Origins of Rotation in Tornadoes Experiment (VORTEX2). All simulated supercells evolving in the near-field environment produce a tornado, and 33% of supercells evolving in the far-field environment produce a tornado. Composite differences between the two ensembles are shown to address storm-scale characteristics and processes impacting the volatility of tornadogenesis. Storm-scale variability in the ensembles is illustrated using empirical orthogonal function analysis, revealing storm-generated boundaries that may be linked to the volatility of tornadogenesis. Updrafts in the near-field ensemble are markedly stronger than those in the far-field ensemble during the time period in which the ensembles most differ in terms of tornado production. These results suggest that storm-environment modifications can influence the volatility of supercellular tornadogenesis.

KEYWORDS: Supercells; Tornadoes; Storm environments; Empirical orthogonal functions

Supplemental information related to this paper is available at the Journals Online website: https://doi.org/10.1175/MWR-D-20-0147.s1.

[a] Current affiliation: Cooperative Institute for Mesoscale Meteorological Studies, Norman, Oklahoma.

Corresponding author: Matthew Flournoy, matthew.flournoy@noaa.gov

DOI: 10.1175/MWR-D-20-0147.1

1. Introduction

Storm-scale characteristics and processes necessary for tornadogenesis in supercells include 1) a low-level,[1] rotating updraft; 2) near-surface[2] rotation; and 3) significant intensification of that near-surface rotation to tornadic intensity at the surface (Davies-Jones 2015). Our current understanding of each of these characteristics differs. The formation of the rotating updraft, or mesocyclone (Barnes 1978; Doswell and Burgess 1993; Glickman 2000), is well understood, at least at midlevels.[3] Horizontal vorticity in the near-storm environment is tilted into the vertical and stretched by a convective updraft (Rotunno 1981; Lilly 1982; Davies-Jones 1984; Dahl 2017). The spatial correlation between vertical velocity and vorticity increases as the angle between the environmental horizontal vorticity vector and wind vectors decreases (i.e., as the streamwise horizontal vorticity component increases; Davies-Jones 1984). Forecasters use storm-relative helicity (SRH), a measure of the amount of the cumulative streamwise vorticity in a certain layer of the atmosphere, to help diagnose environments that are more kinematically conducive for the development of rotation in convective updrafts (e.g., Thompson et al. 2003, 2007). These same processes are also thought to be responsible for the formation of the low-level mesocyclone in a few observational (Markowski et al. 2012a) and modeling studies (Markowski and Richardson 2014; Coffer and Parker 2015, 2017, 2018; Coffer et al. 2017). Additionally, baroclinic generation within the storm can augment the environmental vorticity along parcel trajectories entering the updraft (Klemp and Rotunno 1983; Rotunno and Klemp 1985; Markowski et al. 2012b; Dahl et al. 2014; Orf et al. 2017).

Mechanisms influencing the formation of near-surface rotation have been the focus of many modeling and observational studies. A few processes may contribute, including baroclinic vorticity generation and tilting in storm-scale downdrafts (e.g., Davies-Jones and Brooks 1993; Wicker and Wilhelmson 1995; Markowski and Richardson 2009; Dahl et al. 2014; Markowski and Richardson 2014; Parker and Dahl 2015) and the generation and modification of vorticity via surface friction (Schenkman et al. 2014; Roberts et al. 2016). Regardless of the processes at work, unless preexisting near-surface vertical vorticity is present, a downdraft is theorized to be required for the development of near-surface vertical vorticity (Davies-Jones 1982a,b). Numerous observations exist of rear-flank downdrafts (RFDs; Markowski et al. 2002) and downdrafts associated with descending reflectivity cores (Rasmussen et al. 2006; Markowski et al. 2012a,b, 2018) in the vicinity of tornadoes. To complicate matters, some observational and modeling studies have shown similarities between near-surface kinematic fields in tornadic and nontornadic supercells (e.g., Trapp 1999; Wakimoto and Cai 2000; Markowski 2008; Markowski et al. 2011; Coffer et al. 2017). Given that "the only fundamental requirement for downdrafts to produce surface vertical vorticity is the existence of downdraft-relative flow" (Parker and Dahl 2015), near-surface vertical vorticity probably exists in the vast majority of, if not all, supercells. Thus, it is likely that a deciding factor in tornadogenesis is not whether near-surface vertical vorticity exists, but how that vorticity is modified by the supercell.

In the final moments of tornadogenesis, an intense, low-level updraft stretches near-surface vertical vorticity and wind speeds increase to tornadic intensity. The resulting magnitude of vertical vorticity stretching is related to the strength of the low-level updraft, because vertical velocities vanish to zero at the ground. The buoyancy of near-surface air within which the stretched vorticity resides also plays a role in modulating vertical vorticity tendency (e.g., Markowski and Richardson 2014); generally, more buoyant air experiences larger upward displacements due to vertical pressure perturbation gradient forces associated with the low-level updraft, and the opposite is true for less buoyant air. Storm outflow buoyancy is at least partially related to low-level, environmental moisture content (Rasmussen and Blanchard 1998; Rasmussen 2003; Thompson et al. 2003; Craven and Brooks 2004), with lower lifted condensation levels (LCLs) favoring less negatively buoyant outflow. The physical reasoning for this relationship involves less evaporational cooling in more humid environments (Kumjian 2011; French et al. 2015). This in turn is more favorable for tornadogenesis than supercells with more negatively buoyant outflow (Markowski et al. 2002). In nontornadic supercells, it appears that the low-level updraft fails to draw air upward far from the surface (e.g., Markowski and Richardson 2014; Coffer and Parker 2017), suggesting the presence of a weaker or less steady low-level updraft and/or more negatively buoyant outflow. Recent studies have also found that increased spatial overlap between the surface circulation maximum and low- and midlevel mesocyclones, modulated by low-level wind shear (Guarriello et al. 2018) and humidity (Brown and Nowotarski 2019) in the environment, increases tornado potential.

[1] In this paper, "low-level" roughly refers to the 0–1 km AGL layer or to the 1 km AGL level.

[2] In this paper, "near-surface" roughly refers to the lowest tens of meters AGL.

[3] In this paper, "midlevels" roughly refers to the 3–6 km AGL layer.

Some severe weather outbreaks conducive for supercells are characterized by nearly every supercell producing a tornado, while others may include both tornadic and nontornadic supercells in close proximity to each other (e.g., Klees et al. 2016; Markowski and Richardson 2017). The reason for the latter may be due to mesoscale differences in the background environment (e.g., Markowski et al. 1998; Klees et al. 2016), stochasticity in storm-scale features and evolution (e.g., Coffer et al. 2017), or a combination of both. Specifically, Coffer et al. (2017) examined the "volatility of tornadogenesis" in composite tornadic and nontornadic supercell environments (Parker 2014) sampled during VORTEX2 (Wurman et al. 2012). The study used high-resolution Cloud Model 1 (CM1; Bryan and Fritsch 2002) experiments to create two 15-member ensembles that simulated supercells in both of these environments. All 15 of the supercells initialized in the tornadic near-field environment produced a tornado (defined in Coffer et al. 2017), and six produced a tornado in the nontornadic near-field environment. Thus, at least in simulations, the tornadic environments sampled during VORTEX2 appear to be *strongly* favorable for tornadogenesis regardless of storm-scale stochasticity, while the sampled nontornadic environments appear to be *conditionally* favorable for tornadogenesis given fortunate (or unfortunate) variations in storm-scale features. The difference in tornado production between the simulated storms was mostly attributed to variations in rotation-induced dynamic lift, with storms initialized in the tornadic environment containing stronger low-level updrafts than those in the nontornadic environment. This difference was related to variations in the environmental low-level wind profile in both environments; while both contained similar effective SRH, the tornadic environment was characterized by more streamwise horizontal vorticity (and SRH) in the lowest 500 m AGL than the nontornadic environment (e.g., Thompson and Edwards 2000; Esterheld and Giuliano 2008; Coffer et al. 2019). Tilting and subsequent stretching of this vorticity resulted in the development of a longer-lived, more intense low-level updraft in the tornadic environment.

In this study, we explore the volatility of tornadogenesis further by analyzing an ensemble of simulations in the near- and far-field composite tornadic environments from VORTEX2 (Coffer et al. 2017 only examine the near-field environment in their simulations). As described in Parker (2014), the tornadic near-field environment was extracted roughly 40 km upstream of the supercell updraft in the inflow region—the same as in Coffer et al. (2017)—whereas the far-field environment was extracted roughly 80 km upstream (see Fig. 1). Comparing these two environments allows us to address a couple of questions in addition to those presented in Coffer and Parker (2017, 2018) and Coffer et al. (2017). In particular, we are interested in how the spatial evolution from the far-field to the near-field environments impacts the volatility of tornadogenesis and how kinematic differences impact this volatility. With this in mind, this study aims to address the following questions:

1) What patterns of variability in storm characteristics and tornado potential exist between storms forming in essentially the same environment?
2) Is the volatility of tornadogenesis different in the near- and far-field tornadic VORTEX2 environments?
3) If so, what drives differences in the volatility of tornadogenesis in these environments?

2. Data and methods

a. Model setup

The simulations used in this study were created using CM1 release 19.5. CM1 is an idealized, three-dimensional, nonhydrostatic model useful for studying small-scale atmospheric phenomena such as supercell thunderstorms and tornadoes. Important model settings are discussed next and the full "namelist.input" file is available online as supplemental material. Simulated storms were initiated in horizontally homogeneous environments using the updraft nudging technique outlined in Naylor and Gilmore (2012). Rather than a warm bubble, this technique applied a volume of updraft characterized by a maximum vertical velocity of $15\,m\,s^{-1}$ at 1.5 km AGL at the beginning of the simulation. This nudging diminished with horizontal and vertical extent and was applied consistently for 15 min before exponentially decreasing toward $0\,m\,s^{-1}$ 20 min into the simulation. Each simulation was run for 2 h.

A stretched 200 km × 200 km horizontal grid was used with a minimum grid spacing of 125 m in the inner 100 km × 100 km domain stretched to 3875 m on the edges. Grid motion was set to the approximate storm motion in order to keep each simulated storm near the center of the grid. 115 vertical levels were present, with vertical grid spacing stretching from 20 m in the lowest 300 m AGL to 280 m at the model top (18 160 m). The lowest model level was 10 m AGL. We used a large time step of 0.5 or 0.6 s, depending on the stability requirements of the particular ensemble member,[4] along with a fifth-order advection scheme. The National Severe

[4] Each member was run using a large time step of 0.6 s. If that failed, it was rerun with a 0.5 s time step.

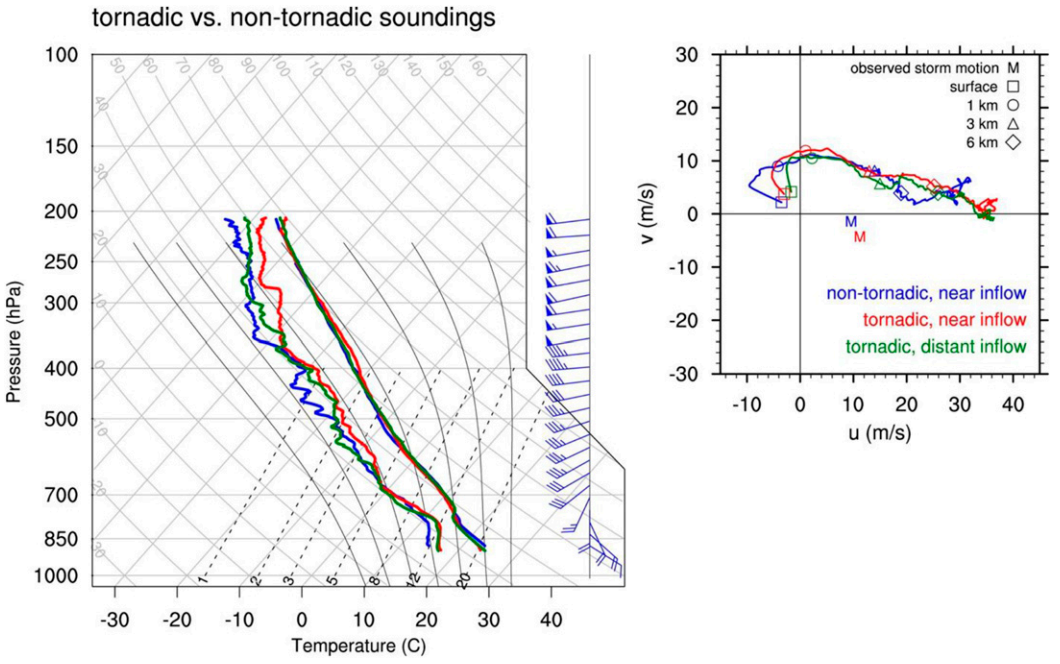

FIG. 1. Soundings extracted from composite environments sampled during VORTEX2 in the vicinity of tornadic and nontornadic supercell thunderstorms (from Parker 2014). The mean storm motion of all tornadic storms is indicated by the red "M," and the mean storm motion of all nontornadic storms is indicated by the blue "M." Near-inflow (far-inflow) soundings were extracted roughly 40 (80) km away from the storm updraft. Tornadic (nontornadic) soundings were extracted from the composite environment sampled in the vicinity of tornadic (nontornadic) supercells.

Storms Laboratory (NSSL) two-moment microphysics scheme was used (Ziegler 1985; Mansell 2010; Mansell et al. 2010) and a semislip condition was applied to the bottom boundary with a constant drag coefficient (C_d) of 0.0014. This value is consistent with a few recent simulation studies (Coffer and Parker 2017, 2018; Coffer et al. 2017) and was derived from the rear-flank outflow composite sounding shown in Parker (2014). Since simulated surface drag may excessively modify near-ground vertical wind shear (Markowski and Bryan 2016), we applied this small constant drag coefficient to our simulations in the hope of increasing physical realism and to more directly compare our results with recent modeling studies. In an effort to best preserve the base-state environment, the Coriolis force was applied to the perturbation winds (e.g., Roberts et al. 2016). After some of the small, erratic kinks in the hodograph (introduced by the ensemble configuration method) were smoothed in the first 5–10 min, the base-state profile was essentially conserved in the far-field environment of the supercell for the rest of the simulation.

b. *Ensemble configuration*

The composite, tornadic near-field (far-field) thermodynamic profile found in Parker (2014) was used as the base-state thermodynamic profile for each member of the near-field (far-field) ensemble (shown by the red and green lines in Fig. 1). The base-state wind profile for each member in the near-field (far-field) tornadic ensemble was generated by perturbing the composite near-field (far-field) tornadic wind profile observed in VORTEX2 (Parker 2014). The original composite wind profiles are bolded in Fig. 2. Commonly used parameters that describe storm environments were calculated using SHARPpy (Blumberg et al. 2017) are shown in Table 1; unsurprisingly, both exhibit characteristics typical of environments in the vicinity of tornadic supercells, although the significant tornado parameter and supercell composite parameter in the near-field environment are larger. This is due to the larger low-level shear and storm-relative wind magnitudes in the near-field environment, resulting in greater SRH.

Perturbations applied to the wind profile were randomly drawn from a uniform distribution of velocities ranging from -2 to $2\,\mathrm{m\,s^{-1}}$ and applied to each vertical level (115 total) of the wind profile. The velocity range of $\pm 2\,\mathrm{m\,s^{-1}}$ was chosen to best represent radiosonde observational error and sampling inconsistencies (e.g., Dawson et al. 2012) and the average of all perturbations applied to any profile was essentially zero. This resulted in two ensembles (near-field and far-field) consisting of 15 members each. Each ensemble consisted of one control member with a base-state wind profile characterized by

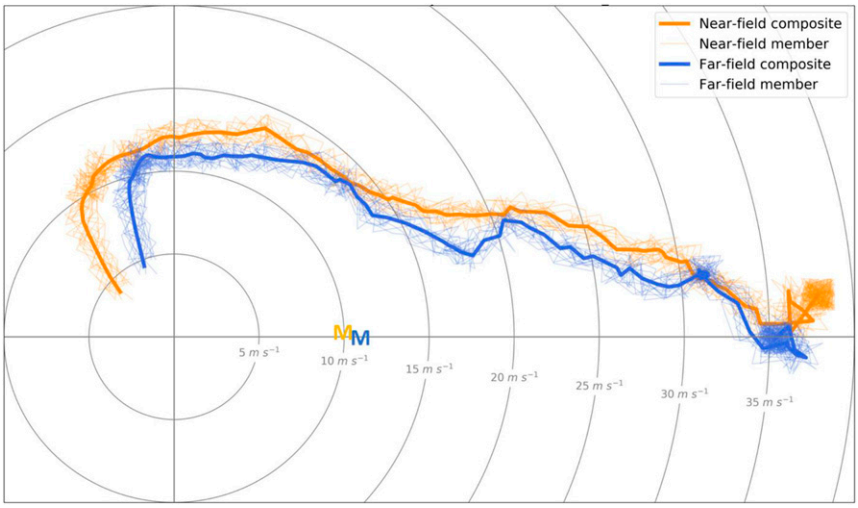

FIG. 2. The tornadic near-inflow (thick orange line) and far-inflow (thick blue line) control hodographs (also shown in Fig. 1) used in this study. Thin lines indicate the 14 hodographs, derived from each control hodograph, used as the base-state, homogeneous wind profile in each ensemble member. The mean storm motion of all supercells in the near-field ensemble is indicated by the orange "M," and the mean storm motion of all supercells in the far-field ensemble is indicated by the blue "M."

the nonperturbed sounding from Parker (2014) and 14 members with slightly perturbed base-state wind profiles as described above (Fig. 2). The only difference between each member in the near- or far-field ensemble is the background wind profile. The thermodynamic profiles used to represent each member in each ensemble were identical, and the thermodynamic profiles differed only slightly between the near- and far-field composite environments (see Fig. 1). Differences between these two ensembles (i.e., interensemble differences) yield insight into the sensitivity of tornadogenesis to different environmental characteristics, and differences within the ensembles (i.e., intraensemble differences) yield insight into the sensitivity of tornadogenesis to different storm-scale characteristics (i.e., the practical predictability).

c. *Definition of tornado genesis and failure*

Because our simulation setup is almost identical to that of Coffer and Parker (2017, 2018) and Coffer et al. (2017), we use the same criteria to define the occurrence of tornado genesis and failure. A tornado is defined when grid points with

1) 10 m AGL vertical vorticity $\geq 0.3\,s^{-1}$,
2) 0–1 km AGL pressure perturbations ≤ -10 hPa, and
3) 10 m AGL wind speeds $\geq 35\,m\,s^{-1}$ (low-end EF0),

occur within 4 km of each other for at least two consecutive minutes (using output every minute). The time of tornadogenesis is defined as the first time these criteria are met. If these criteria are not met during the 2-h simulation, the time of tornado failure is defined as the time of maximum 10 m AGL vertical vorticity.

d. *EOF analysis*

To analyze spatial patterns of variance in the simulated supercells, empirical orthogonal function (EOF; Lorenz 1956) analysis was performed on different output variables. This type of composite analysis has previously

TABLE 1. Commonly used parameters associated with the tornadic near- and far-field composite VORTEX2 environments. Convective available potential energy (CAPE; J kg^{-1}), convective inhibition (CIN; J kg^{-1}), and lifted condensation level (LCL; m) are all calculated using the surface-based (SB) parcel. 0–1 and 0–3 km SRH ($m^2\,s^{-2}$) are shown as well as SRH calculated within the effective layer (CAPE > 100 J kg^{-1} and CIN > -250 J kg^{-1}) of the storm (ESRH; $m^2\,s^{-2}$). Critical angle is calculated as the angle (in degrees) between the 10 m AGL storm-relative wind vector and the 10–500 m AGL shear vector (as defined in Esterheld and Giuliano 2008). The significant tornado parameter (STP; dimensionless) and supercell composite parameter (SCP; dimensionless) are also calculated as defined in Thompson et al. (2007).

	SB CAPE	SB CIN	SB LCL	0–1 km SRH	0–3 km SRH	ESRH	Critical angle	SCP	STP
Near-field	2566	−71	734	255	331	298	86	16.9	4.8
Far-field	2644	−62	842	159	267	222	81	12.8	2.8

been performed in meteorological studies (e.g., Richman 1980) and used in severe weather studies primarily to analyze synoptic-scale patterns supportive of tornadoes (e.g., Schaefer and Doswell 1984; Mercer et al. 2012). Using this technique, large datasets are reduced to a smaller set of normal characteristic patterns, or EOFs. In this study, singular value decomposition (e.g., Bretherton et al. 1992) was used to compute the principal component (PC) time series. Spatial patterns of the fields were then obtained by regressing the original spatial field of each variable within 10 km of the near-surface vortex with the corresponding standardized leading PC time series. The leading EOF pattern (EOF1) explains the largest fraction of variance in the original dataset and subsequent EOF patterns explain decreasing fractions of variance. While the orthogonal nature of the EOFs limits their applicability to the real atmosphere, we examine EOF1s that explain the most variance and are aligned with known, physical features.

This study examines EOF patterns of simulated variables in the near- and far-field ensemble at the time of tornado genesis or failure, including near-surface vertical vorticity (ζ), density potential temperature perturbation (θ'_ρ), and wind direction. This approach differs from most meteorological applications of EOF analysis in that the grid spacing is smaller (125 m) and the number of input datasets is smaller (15 for each EOF pattern for each ensemble). As will be discussed in the next section, some EOFs in this study contain significant small-scale structure due to the small grid spacing used and turbulence present in the simulated storm outflow. However, insight can be drawn from examining regions of the domain characterized by greater or lesser amplitudes of small-scale variability and where demarcations between these two regions are present. Due to the small number of input datasets and the fact that time or spatial means were not subtracted from the dataset, EOF1s that explain a large amount of variance will appear similar to a composite map constructed by simple ensemble averaging. Regardless, the EOF analysis will yield leading patterns of variance for each field in addition to providing analytical support for spatial patterns that emerge in each 15-member ensemble.

3. Results

a. Bulk ensemble characteristics

Every member of both the near- and far-field ensembles develops a right-moving supercell with similar aggregate characteristics during the 2-h simulation. This supercell develops around 40–50 min into each simulation. By the time of tornado genesis or failure, classic observed and simulated supercellular characteristics are evident in each member, including a reflectivity hook and strong midlevel updraft (Figs. 3 and 4). These supercells remain discrete for the remainder of the 2-h simulation.

The two ensembles differ in terms of tornado production. Based on the criteria (described in section 2c), all near-field ensemble members produce a tornado and five far-field ensemble members produce a tornado. Figure 3 shows surface[5] reflectivity and the location of the midlevel updraft for each ensemble at the time of tornadogenesis in each near-field ensemble member (ranging from 49 to 56 min). Although all members are initialized in essentially the same environment (Fig. 2), each storm is slightly different (as expected, given the nature of error growth on convective scales; Cintineo and Stensrud 2013). In general, all storms contain a strong midlevel updraft bounded by a hook echo to the west (more evident in some members than others) and large reflectivity to the north.

Reflectivity hook echoes and midlevel updrafts are also present in the far-field ensemble at the time of tornado genesis or failure, although they are not as pronounced in all of the individual members (Fig. 4). Compared to the near-field ensemble, some midlevel updrafts are weaker and smaller (e.g., Figs. 4e,j), but overall the reflectivity and midlevel updraft presentation does not differentiate well between the tornadic and nontornadic members within the far-field ensemble. In particular, some midlevel updrafts in nontornadic members (e.g., Fig. 4o) appear just as strong and expansive as those in tornadic members (e.g., Fig. 4n).

Surface outflow characteristics also differ between the two ensembles at the time of tornado genesis or failure (Figs. 5 and 6). Both ensembles contain very cold ($\theta'_\rho \leq -5$ K) surface air by this time in the rear-flank downdraft—consistent with the observational analyses of Markowski et al. (2002)—and cool air ($\theta'_\rho \sim -1$ to -3 K) in the forward-flank region to the east. However, the coldest outflow is generally constrained farther northwest, away from the surface vortex in the near-field ensemble (Fig. 5) than in the far-field ensemble (Fig. 6). Localized, zonally oriented cooling due to forward-flank precipitation is also more evident in the near-field ensemble than in the far-field ensemble (e.g., Fig. 5i). Some of this is due to the smaller range of tornadogenesis (or failure) times in the near-field ensemble than those in the far-field ensemble (these times are indicated at the bottom left of the figure panels). However, some far-field members that produce strong surface vortices earlier in their life

[5] In this paper, "surface" refers either to the surface or the lowest model level (10 m AGL).

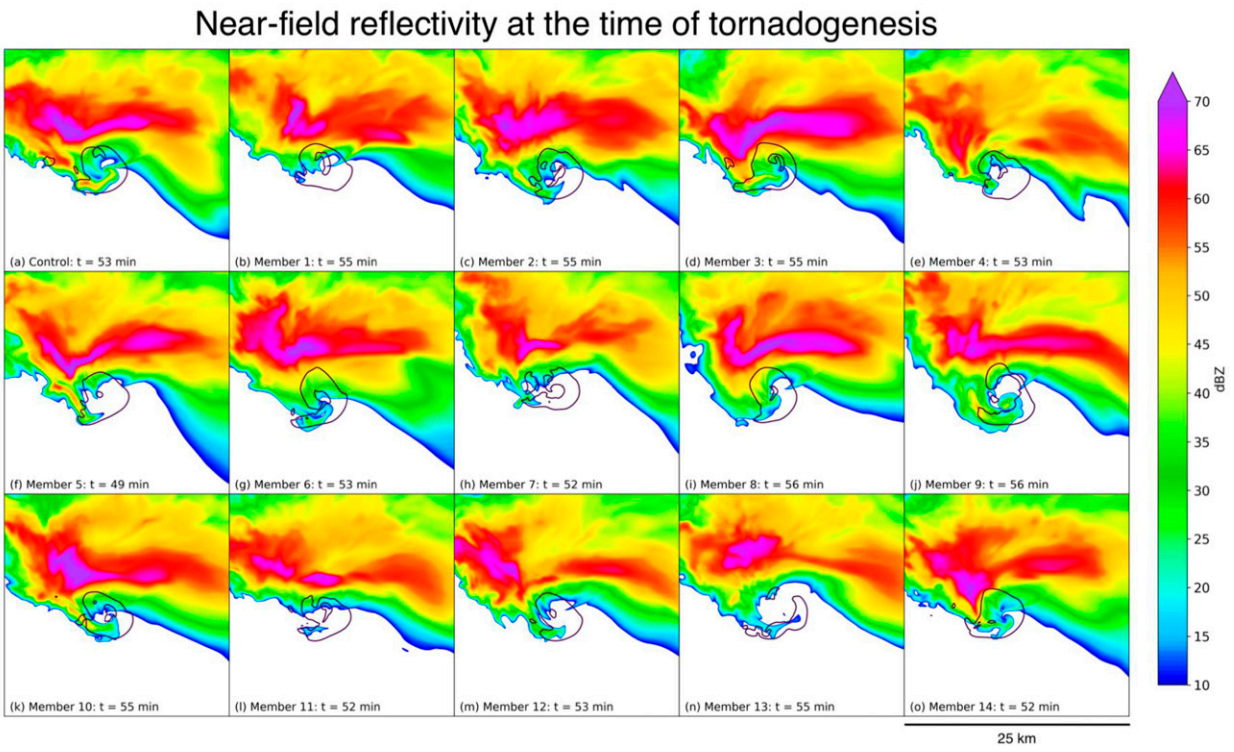

FIG. 3. Simulated radar reflectivity (10 m AGL, shaded) and updraft (20 m s^{-1} at 3 km AGL, black contour) in the 15 near-field ensemble members. Variables are plotted at the time of tornadogenesis. These times are indicated in the bottom-left corner of each panel.

cycle do not exhibit localized forward-flank cooling like the near-field members (e.g., Figs. 6e,h,j,l).

Time series of 1 km AGL updraft flux, minimum surface θ'_ρ, and maximum surface ζ within a 50 km^2 domain centered on the midlevel updraft of the supercell in each ensemble member are presented in Fig. 7. Median ζ in the near-field ensemble is slightly larger than that in the far-field ensemble until around t = 50 min (Fig. 7a). At this point, maximum surface vertical vorticity magnitudes increase dramatically in the near-field ensemble to over twice those in the far-field ensemble around t = 55 min. Thereafter, near-field magnitudes generally decrease until around t = 100 min. Meanwhile, maximum surface vertical vorticity magnitudes in the far-field ensemble are not nearly as peaked and gradually increase until around t = 75 min. After this point, the two distributions remain similar until around t = 105 min when the near-field median grows slightly larger than the far-field median through the rest of the simulation period.

1 km AGL updraft fluxes are stronger in the near-field ensemble than in the far-field ensemble (Fig. 7b). This difference is present from the beginning of the time period and peaks around t = 55–60 min (during tornado production in all near-field members). At this point, updraft fluxes in the near-field ensemble are 6–7 times stronger than those in the far-field ensemble. Afterward, 1 km AGL updraft fluxes in the near-field ensemble gradually decrease until around t = 85–90 min, at which point they increase again until the end of the simulations. Both increases in near-field updraft fluxes (t = 40–50 and 85–120 min) begin several minutes before an increase in maximum surface vertical vorticity magnitudes (t = 50–55 and 100–120 min). Meanwhile, far-field updraft fluxes gradually increase until around t = 70 min and remain constant thereafter.

Minimum surface θ'_ρ is similar between the ensembles through around t = 70 min (Fig. 7c). Based on the time series, cold downdrafts reach the surface in both ensembles at the same time, around t = 40–45 min. During the next few minutes, θ'_ρ in both ensembles decreases by 2–4 K and gradually warms until around t = 75 min. At this time, median values of the minimum θ'_ρ in the near-field ensemble are around 0.5–1 K warmer than those in the far-field ensemble. After t = 75–80 min, a second round of cold downdrafts reaches the surface that results in decreasing θ'_ρ in both ensembles until t = 90–100 min. The minimum surface θ'_ρ is substantially lower in the far-field ensemble during this period.

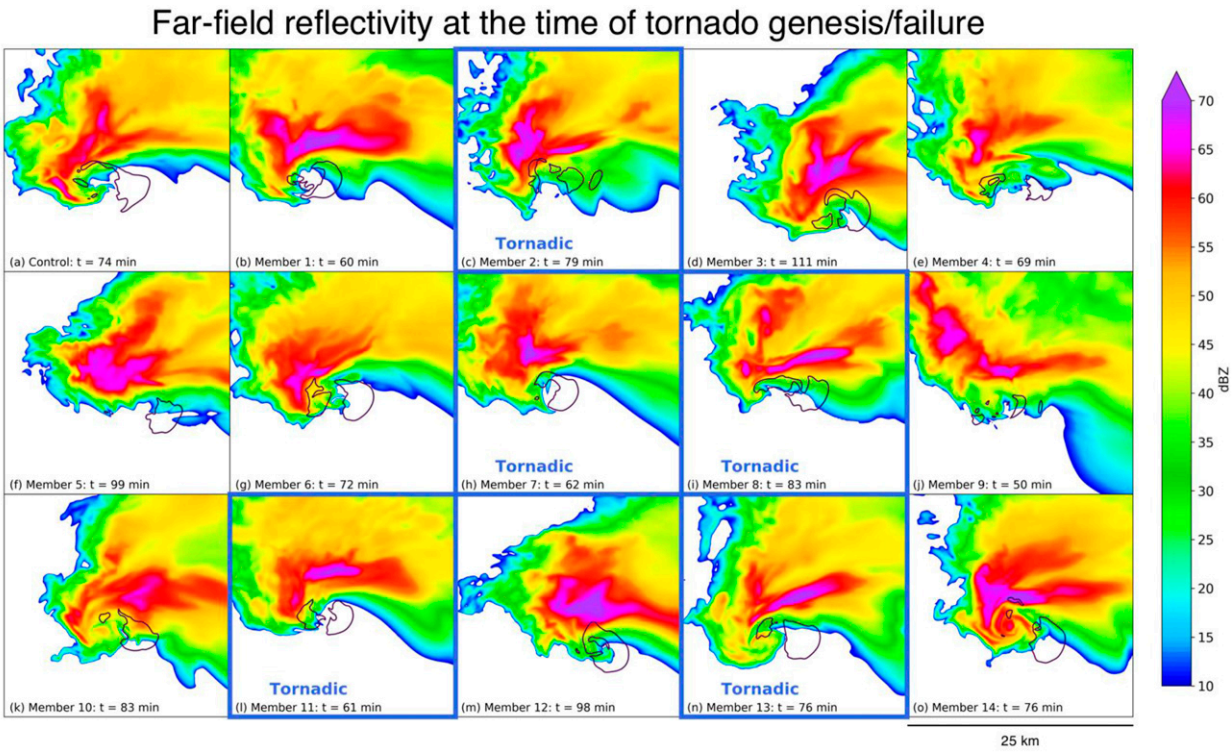

FIG. 4. As in Fig. 3, but for the 15-member far-field ensemble. The five tornadic members are outlined in blue.

These bulk ensemble characteristics reveal a few key relationships between the ensembles (Fig. 7). First, the interquartile range is generally similar in both ensembles. This suggests that the influence of intrastorm processes (i.e., those not strongly governed by the background environment) on supercell characteristics is similar in both composite VORTEX2 environments. Next, at least in the near-field ensemble, increases in low-level updraft flux occur simultaneously with decreases in surface θ'_ρ (t = 45–50 and 80–100 min), which precede increases in surface vertical vorticity. Finally, some of the signals in the ensembles are similar but lagged in time. In particular, the near-field ensemble rapidly peaks in surface vertical vorticity magnitudes and low-level updraft fluxes around t = 55 min, and those in the far-field ensemble gradually increase and peak around t = 70–75 min. Perhaps this is evidence of larger streamwise vorticity in the background environment (Fig. 2) supporting more rapid low-level mesocyclone development and, in this case, a peak in tornado potential earlier in the storms' life cycles. On the other hand, the second round of cold downdrafts reach the surface 5–10 min earlier in the far-field ensemble (t = 70–75 min) than in the near-field ensemble (t = 80 min). Ultimately, although the observed hodographs were both associated with tornadic storms in VORTEX2, the character of the simulated ensembles is different enough that one ensemble is significantly more supportive of long-lived, intense surface vortices.

b. *Storm-scale characteristics influencing tornado genesis and failure*

To assess what local factors influence tornado genesis or failure in the ensemble members, mean surface θ'_ρ and maximum 1 km AGL vertical velocities within 4 km of the surface vortex are analyzed. Figure 8 shows violin plots of these variables during the 10-min period leading up to tornado genesis or failure (i.e., the times indicated in Figs. 3 and 4). Unsurprisingly, 1 km updrafts near the developing vortex are stronger in the near-field ensemble during most of the 10-min period (Fig. 8a). The difference between the medians of these distributions is statistically significant at the 90% confidence level at $t - 2$ and at $t = 0$ using a Monte Carlo test with 10 000 iterations. This difference maximizes at the time of tornado genesis or failure. Low-level updrafts strengthen in both ensembles from $t - 10$ to $t - 2$, but in the final minutes preceding tornado genesis or failure, updrafts in the near-field ensemble continue to strengthen while those in the nontornadic far-field members weaken. The five tornadic far-field members exhibit varying low-level updraft strengths, with some above the distribution of nontornadic far-field members (e.g., Members 2 and 7) and one below (Member 8).

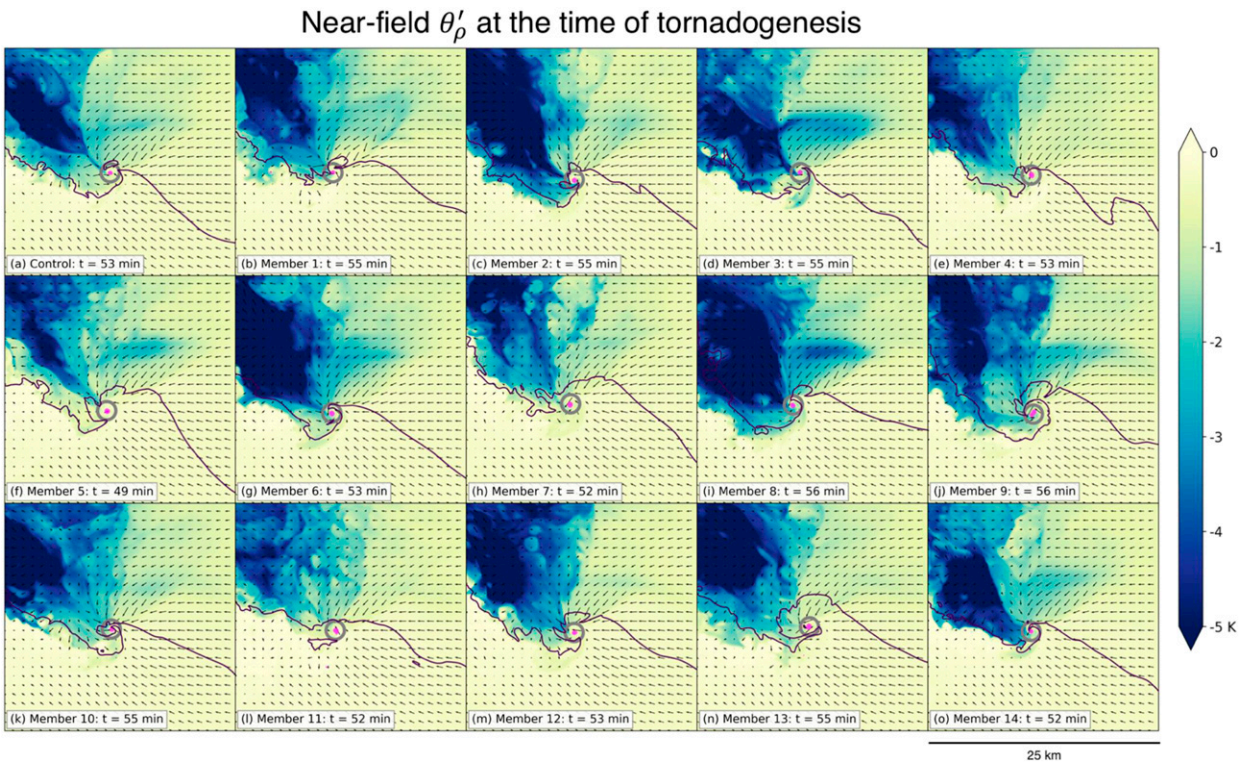

FIG. 5. Simulated surface θ'_ρ (shaded), 10 dBZ reflectivity (solid black line), and storm-relative wind direction (arrows) in the 15 near-field ensemble members. As in Fig. 3, variables are plotted at the time of tornadogenesis for each member. Surface vertical vorticity exceeding 0.1 s^{-1} is shaded in pink, and the surface vertical vorticity maximum is circled for clarity.

Interestingly, all surface vortices in the 10 nontornadic far-field members achieved surface vertical vorticity greater than 0.3 s^{-1} (Fig. 9). Of these 10, 7 members achieved all tornadogenesis criteria except that the vortex was not sustained at that strength for at least 2 min (Members 5, 6, and 9 did not). This vortex evolution shows that *the failure of the far-field ensemble to produce simulated tornadoes was not due to an inability to produce strong vortices, but rather due to an inability to sustain strong vortices.* This may be related to the detrimental presence of weaker low-level updrafts or slightly colder surface outflow in the far-field ensemble, but the physical processes influencing tornadogenesis failure are not explored further in this study.

Differences between the ensembles in terms of storm outflow buoyancy are also evident in Fig. 8b. First, outflow near the developing vortex in the near-field ensemble members is warmer than that in the far-field ensemble. The difference between the medians of both distributions is statistically significant at the 99% confidence level during this time period using a Monte Carlo test with 10 000 iterations. This result is consistent with the understanding that warmer outflow in the vicinity of the vortex (i.e., within 4 km) is associated with increased tornado potential (Markowski et al. 2002). The range of the θ'_ρ distribution is also much smaller in the near-field ensemble, especially in the minutes preceding tornadogenesis. These findings combined with the interpretation of Fig. 7c show that, although the range of outflow temperatures within the entire storm is similar between the two ensembles (e.g., the interquartile range in Fig. 7c), storms in the near-field ensemble more successfully restrain colder air away from the developing vortex, resulting in warmer outflow there than in the far-field ensemble; θ'_ρ in the tornadic far-field members does not differ from the nontornadic members, except for Member 2. It appears the strength of the low-level updraft (the strongest of the far-field ensemble) was sufficient for tornadogenesis within this negatively buoyant outflow. These results also show that, in addition to the presence of stronger low-level updrafts, the success of the near-field ensemble in sustaining intense vortices at $t = 0$ was influenced by warmer outflow in the vicinity of the vortices.

c. *Storm-scale variability within both ensembles*

To further quantify differences between the near- and far-field ensembles and to examine spatial features and processes influencing tornado genesis or demise, EOF1 analysis of surface characteristics are presented next.

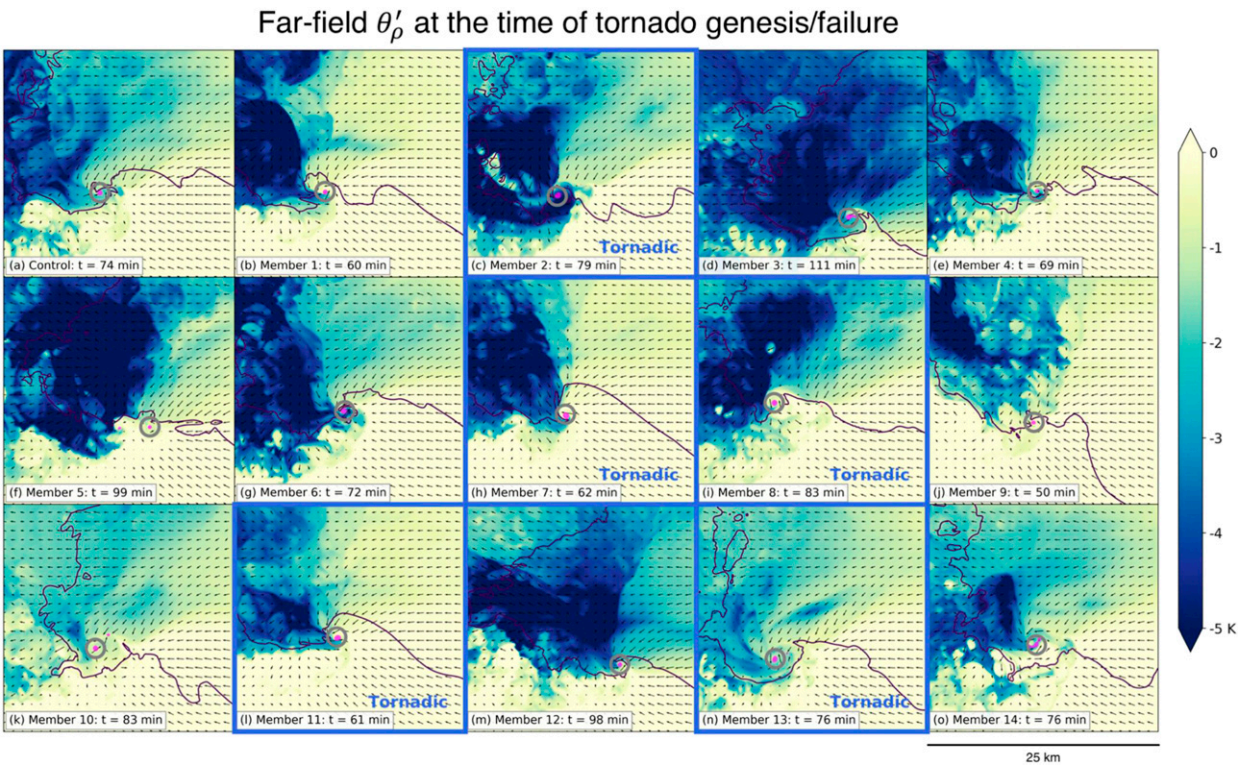

FIG. 6. As in Fig. 5, but for the 15-member far-field ensemble. The five tornadic members are outlined in blue.

Figure 10 shows the regression of surface ζ in the near- and far-field ensembles at the time of tornado genesis or failure. Larger magnitudes of EOF1 (either positive or negative) indicate regions with greater variance within each ensemble, while smaller magnitudes indicate regions with less variance. Regions of large variance with opposing magnitudes indicates that the variance in these regions is anticorrelated. The leading modes explain over 62% and 53% of the variance in the near- and far-field ensembles, respectively. In general, substantial small-scale structure is present in the supercell outflow west of the vortex because ζ is a spatial derivative field and thus is influenced by turbulent flow in these areas. Across the 15-member ensemble, increased (decreased) turbulence will coincide with increased (decreased) variance. Meanwhile, near-zero magnitudes are present in the environment east of the vortex. Large gradients between these regions in both ensembles are subjectively highlighted, including a demarcation extending from the east side of the vortex curling around to the southwest. This is consistent with the location of the rear-flank downdraft gust front in each of the ensemble members (see the storm-relative wind vectors in Figs. 5 and 6). A cyclonic wind shift is also present along the rear-flank gust front with southeasterly environmental winds shifting to near-zero wind speeds within the rear-flank outflow (Fig. 11). [These wind speeds are not actually near-zero in each individual ensemble member (Fig. 5); compositing the large spatial variability in wind direction (Fig. 11a) simply results in a near-zero velocity vector.]

A second boundary appears in both ensembles extending northward from the vortex into the core of the storm (Fig. 10). The gradient in EOF1 magnitudes across it is smaller than that across the rear-flank downdraft, with EOF1 magnitudes increasing to the west. This is consistent with the location of storm-scale boundaries present in some past supercell simulations including left-flank convergence boundaries (Beck and Weiss 2013), vortex sheets (Markowski et al. 2014), vorticity rivers (Dahl et al. 2014; Coffer and Parker 2017), and streamwise vorticity currents (Orf et al. 2017). These boundaries, particularly vorticity rivers and streamwise vorticity currents, have been theorized to increase tornado potential in supercells by either interacting with the low-level updraft or the tornado itself. In this study, this boundary is present in both the tornadic near-field ensemble and largely nontornadic far-field ensemble. It is also present in EOF analyses of vertical vorticity in the 10 nontornadic, far-field members (not shown). It is closer to the surface vortex in the near-field ensemble, whereas in the far-field ensemble it appears farther east.

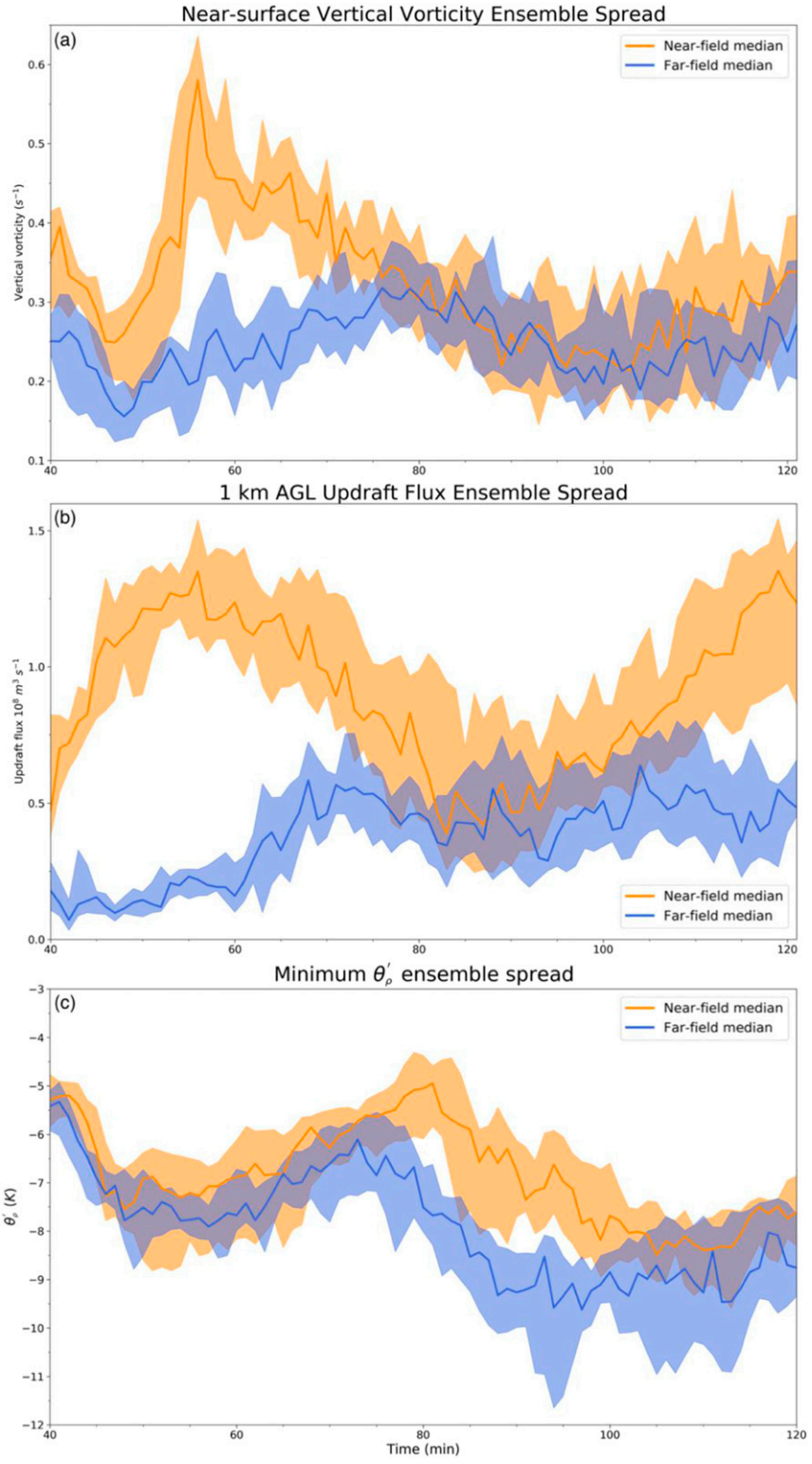

FIG. 7. Time series of (a) maximum surface vertical vorticity, (b) 1-km AGL updraft flux where vertical velocity exceeds 15 m s^{-1}, and (c) minimum surface θ'_ρ within a 50 km^2 domain centered on the midlevel updraft of the right-moving supercell in each ensemble member from 40 to 120 min into the simulation. The first 40 min are excluded due to model spinup. The solid blue (orange) line in each panel indicates the median of the specified variable for the far-field (near-field) ensemble. The blue (orange) shading indicates the interquartile range of the specified variable for the far-field (near-field) ensemble.

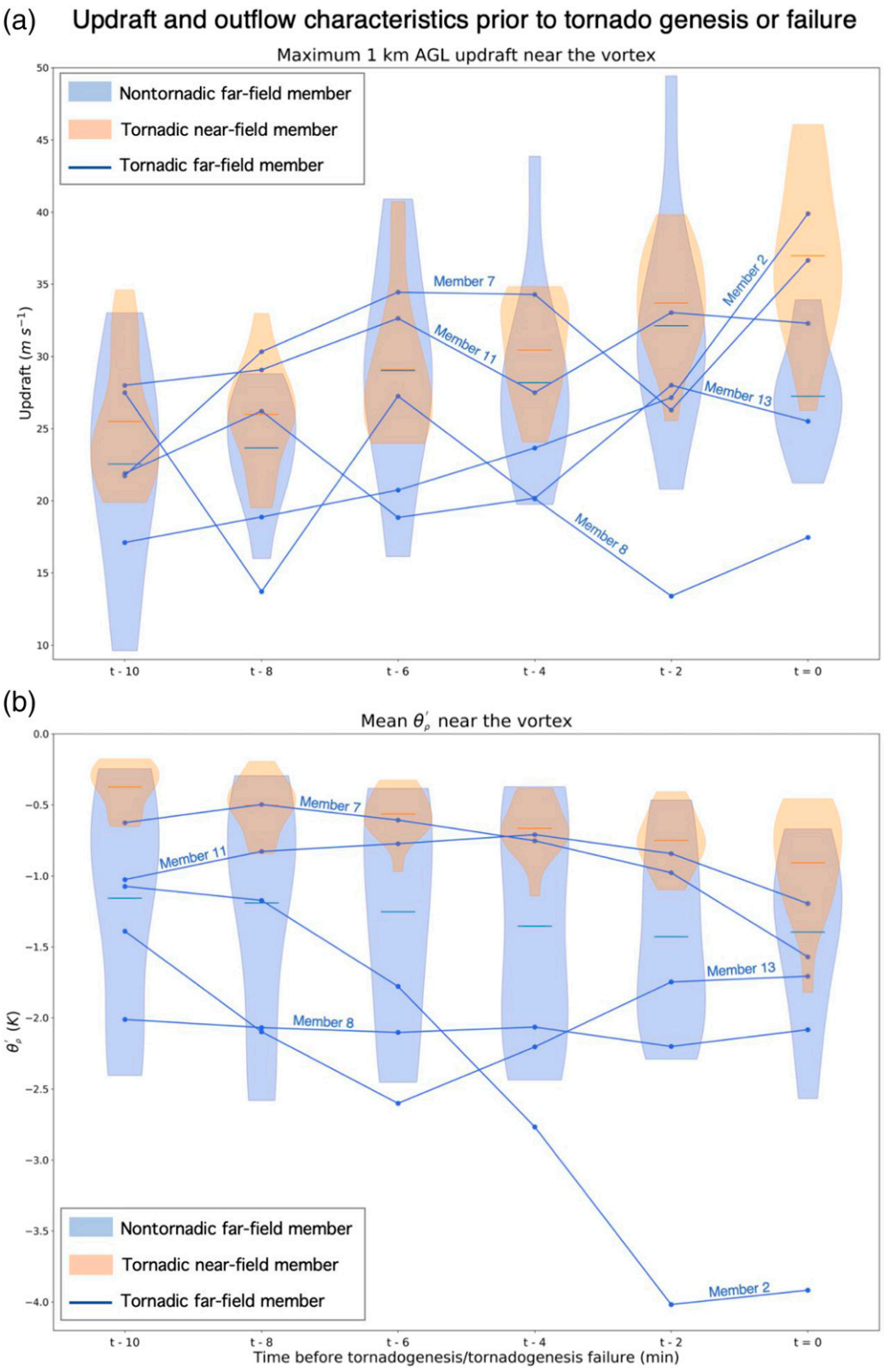

FIG. 8. (a) Violin and scatterplots of 1 km AGL vertical velocity within 4 km of the surface vortex in the near-field (orange) and far-field (blue) ensembles during the 10-min period prior to tornado genesis or failure; "$t = 0$" represents the time of tornado genesis or failure. The near-field violin plots (orange) are composed of maximum vertical velocities from the tornadic members ($n = 15$). The far-field violin plots (blue) are composed of maximum vertical velocities from the nontornadic members ($n = 10$) and the five tornadic members are represented with blue lines. Horizontal lines indicate the median of each distribution. (b) As in (a), but for mean surface AGL θ'_ρ.

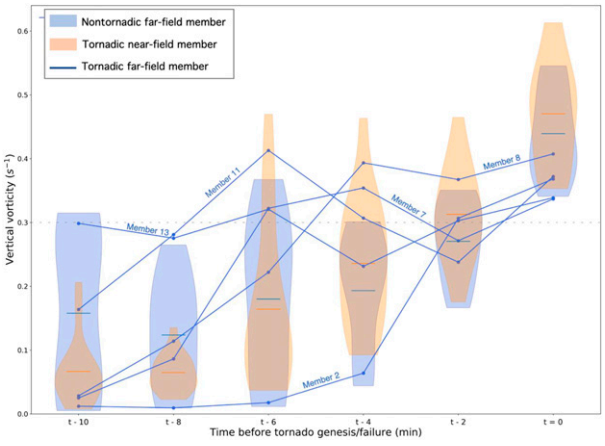

FIG. 9. As in Fig. 8, but for surface ζ; $\zeta = 0.3\,\mathrm{s}^{-1}$ is highlighted because exceeding that value is one of the three criteria for tornado genesis in the simulation. It is a necessary but not sufficient condition.

The physical nature of the demarcations revealed in the vertical vorticity EOF1s (Fig. 10) is examined in Fig. 11 with the characteristic patterns of the leading mode of variability of surface θ'_ρ and storm-relative wind direction. A gradient in θ'_ρ variability is present in both ensembles EOF1 (Fig. 11) along the southern edge of the storm, generally consistent with the location of the rear-flank gust front. This signal is collocated with increased variance in storm-relative wind direction, indicative of varying flow behind the rear-flank gust front in each storm.

Gradients in θ'_ρ and wind direction also exist to the north of the vortex in both ensembles. These gradients are clearer in the near-field ensemble (Fig. 11a). A gradient in the θ'_ρ EOF1 extends northwestward and then northward from the vortex, along with a gradient in storm-relative wind direction to the east (extending due north from the vortex). Both of these features lie to the west of the gradient in ζ EOF1 (Fig. 10a). The region is also characterized by a broad cyclonic wind shift in storm-relative winds (Fig. 11a). These features are not as clear in the far-field ensemble (Fig. 11b). A cyclonic wind shift is present, but any gradients in the θ'_ρ EOF1 in this region are smaller. Increased variance in storm-relative wind direction is present farther west and northwest of the vortex. This gradient is displaced well to the west of the gradient in ζ EOF1 (Fig. 10b).

Finally, the forward-flank region to the northeast of the surface vortex differs between these two ensembles, particular with respect to variance in θ'_ρ. In the near-field ensemble, less variability exists and is spatially confined within the core of the storm (Fig. 11a). This signal is collocated with a zonally oriented region of larger θ'_ρ present in many near-field members (e.g., Fig. 5, all members except for 4, 11, and 13), likely due to evaporative cooling from forward-flank precipitation (e.g., Fig. 3). The orientation of the resulting meridional θ'_ρ gradient with respect to storm-relative winds in this region (Fig. 11a) is consistent with baroclinic reorientation of vorticity along parcels bound for the low-level updraft and/or tornado (e.g., Davies-Jones and Brooks 1993). Increased variance exists in the forward-flank in the far-field ensemble in terms of both the magnitude and spatial extent of the θ'_ρ EOF1; this is related to the lack of consistent forward-flank cooling in the far-field ensemble (Fig. 6). This also applies to the 10 nontornadic far-field members (not shown). As such, it appears that in this region of the storm, critical for processes influencing supercellular tornado potential, more variability exists in the far-field ensemble than in the near-field ensemble.

d. *Low-level vertical pressure perturbation gradient accelerations*

In addition to differences in outflow characteristics and storm-scale variability, we have shown that low-level updraft fluxes are much larger in the near-field ensemble than in the far-field ensemble, especially during the period when all near-field members produce tornadoes (Fig. 7b). To assess factors influencing updraft strength in these simulations, the pressure perturbation field (p') was decomposed into its dynamic (p'_D) and buoyant (p'_B) components. Furthermore, the dynamic component can be expressed as the sum of the linear (p'_L) and nonlinear (p'_{NL}) components. Using these terms, p' can be expressed as

$$p' \propto (e'_{ij})^2 - \frac{1}{2}|\boldsymbol{\omega}'|^2 + 2\left(\frac{\partial w'}{\partial x}\frac{\partial \overline{u}}{\partial z} + \frac{\partial w'}{\partial y}\frac{\partial \overline{v}}{\partial z}\right) - \frac{\partial B}{\partial z}, \qquad (1)$$

where B is the buoyancy, $\overline{u}$ and $\overline{v}$ are the horizontal, base-state wind components, w' is the vertical velocity (note that $\overline{w} = 0$), $\boldsymbol{\omega}'$ is the perturbation vorticity, and e'_{ij} is the stress tensor for the perturbation winds (also called the deformation or the rate-of-strain tensor), which is expressed as

$$e'_{ij} = \frac{1}{2}\left(\frac{\partial u'_i}{\partial x_j} + \frac{\partial u'_j}{\partial x_i}\right). \qquad (2)$$

The first two terms on the right-hand side of Eq. (1) contribute to p'_{NL}, the third represents p'_L, and the fourth represents p'_B (Markowski and Richardson 2010, p. 30). Using the methodology of Hastings and Richardson (2016), p'_L and p'_B are solved using Neumann conditions at the lateral boundaries with a discrete cosine transform and

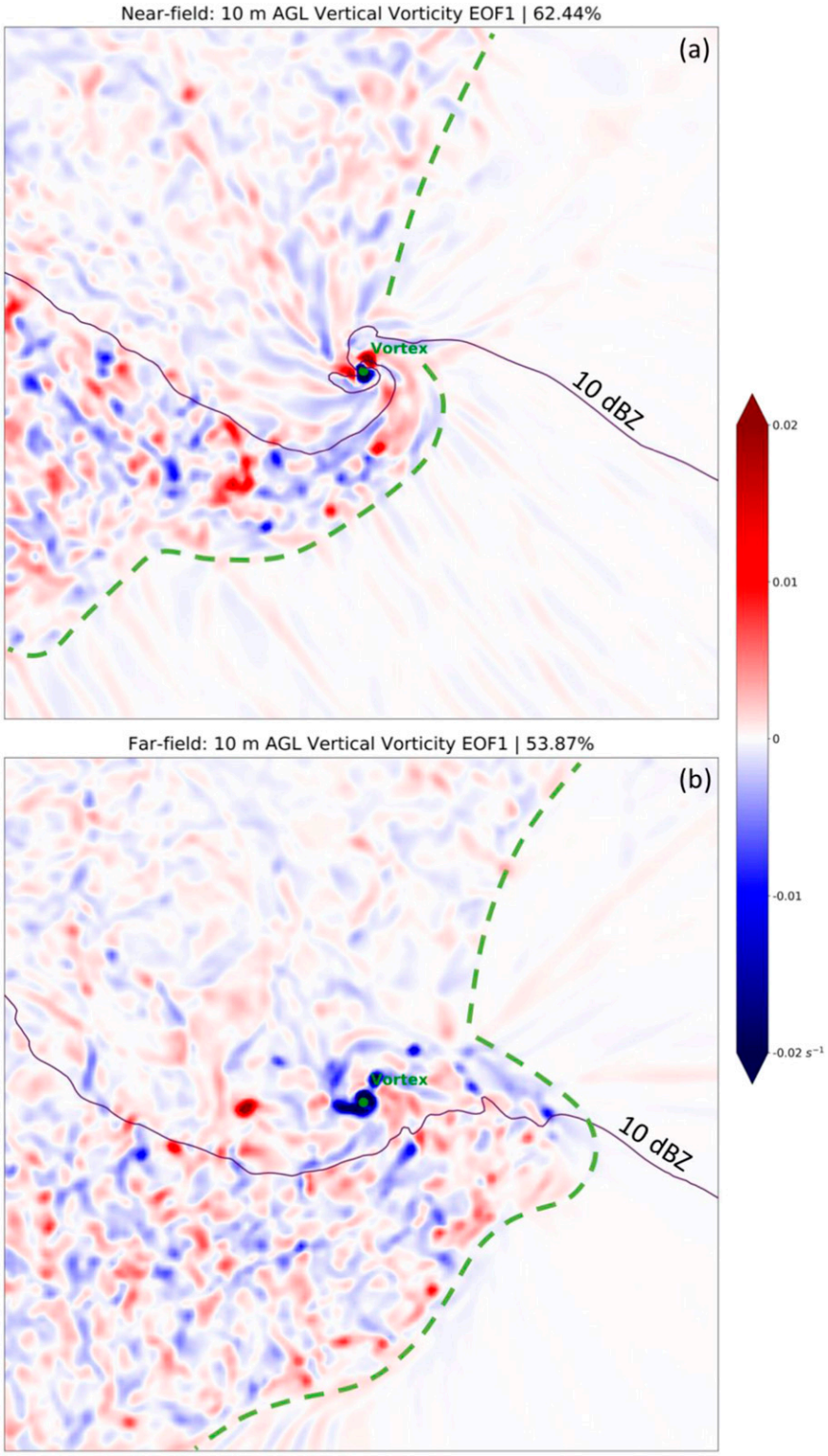

FIG. 10. Regression of 10 m AGL ζ onto the leading standardized PC time series of ζ (shaded) for the (a) near-field ensemble and (b) far-field ensemble in a 20 km × 20 km domain centered on the surface vortex. Ensemble-mean 10 dBZ radar reflectivity at 10 m AGL is contoured in black and the location of the vortex is indicated. PC time series for each ensemble were derived from the 15 ensemble members at the times indicated in Fig. 3. Green dashed lines subjectively indicate local regions with large gradients in the magnitude of the EOF1.

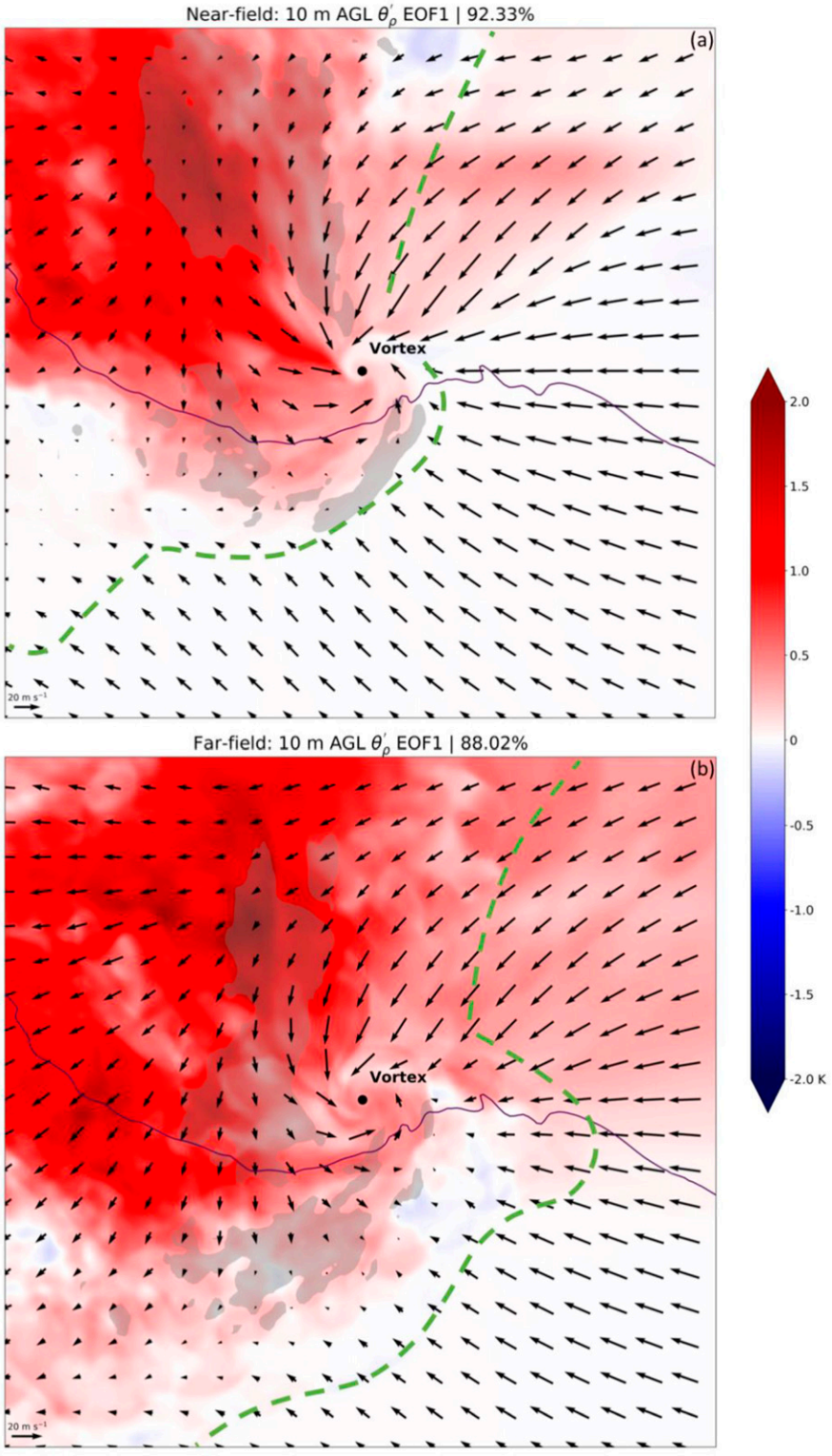

FIG. 11. As in Fig. 10, but for 10 m AGL θ_ρ' (color fill). The gray shading in each plot indicates regions where the regression of the 10 m AGL wind direction field onto their leading PC time series exceeds 50° in each ensemble. Arrows indicate composite, storm-relative 10 m AGL winds for each ensemble at the time of tornado genesis or failure, calculated by averaging the storm-relative winds (centered on the vortex) from all members of that ensemble. The heavy, green dashed lines are identical to those in Fig. 10.

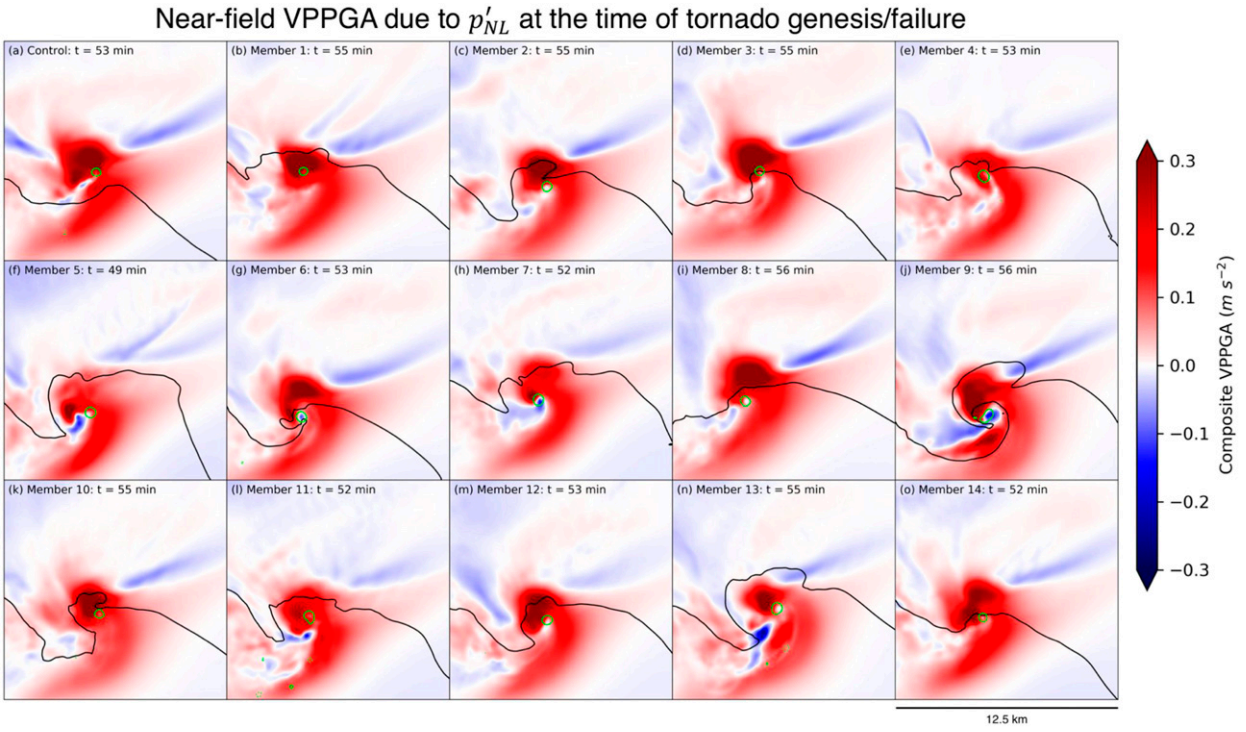

FIG. 12. Composite vertical pressure perturbation gradient acceleration (VPPGA) due to nonlinear, dynamic pressure perturbations (p'_{NL}, shaded), and composite 10 dBZ reflectivity (black contour) in the 15 near-field ensemble members. The VPPGA is composited during the 10 min preceding tornado genesis. As in Fig. 3, variables are plotted at the time of tornado genesis for each member. Surface vertical vorticity exceeding 0.1 s^{-1} at the time of tornado genesis or failure is contoured in green.

boundary conditions at the top and bottom in order to have no vertical accelerations at the surface, $\partial\pi'_L/\partial z = 0$ and $c_p\theta_\rho\partial\pi'_B/\partial z = 0$. Due to nonuniqueness, a constant is added to p'_L and p'_B such that the averages over the domain are zero. p'_{NL} is found as the residual. Last, to examine vertical accelerations due to these terms, the vertical pressure perturbation gradient acceleration (VPPGA) for each term is $(-1/\rho_o)(\partial p'/\partial z)$, where p' refers to the component of interest. In this case, we calculate 0–1 km AGL VPPGAs and composite them in the 10-min period leading up to tornado genesis or failure.

0–1 km AGL composite VPPGAs due to p'_{NL} at the time of tornado genesis or failure for the near-field reveal large, positive accelerations arcing around the east side of the developing vortices. These accelerations are due to the presence of (i) the strong low-level updraft causing large vertical vorticity tendencies aloft [i.e., term 2 in Eq. (1)] and (ii) near-surface convergence at the surface associated with the rear-flank gust front [i.e., term 1 in Eq. (1)]. In some instances, negative VPPGAs are collocated with the surface vortex at the time of tornado genesis or failure (e.g., Fig. 12c). This signal is due to the development of intense ζ at the surface and a corresponding downward VPPGA due to p'_{NL}. Prior to this signal appearing, these vortices develop within the broader region of positive VPPGAs.

Comparing composite VPPGAs due to p'_{NL} in the far- and near-field ensembles yields striking differences (Figs. 12 and 13). While the spatial structures of the VPPGAs in the far-field ensemble are similar to those in the near-field ensemble, they are weaker. This results in weaker updrafts less capable of stretching near-surface vertical vorticity to tornadic strength. Within this ensemble, the five tornadic members generally appear to have stronger VPPGAs due to p'_{NL} than the nontornadic members, although some nontornadic members contain large VPPGAs as well (e.g., Figs. 13k,o).

4. Discussion

The near-field ensemble in this study is configured identically to that in Coffer et al. (2017) except for slight variations in domain size and the version used. All members of the near-field ensemble created in both studies produced tornadoes within minutes of each other, indicating that the error growth arising from infinitesimal differences (like the slight variation in grid size used here) has not yet reached a state in which the storm-scale

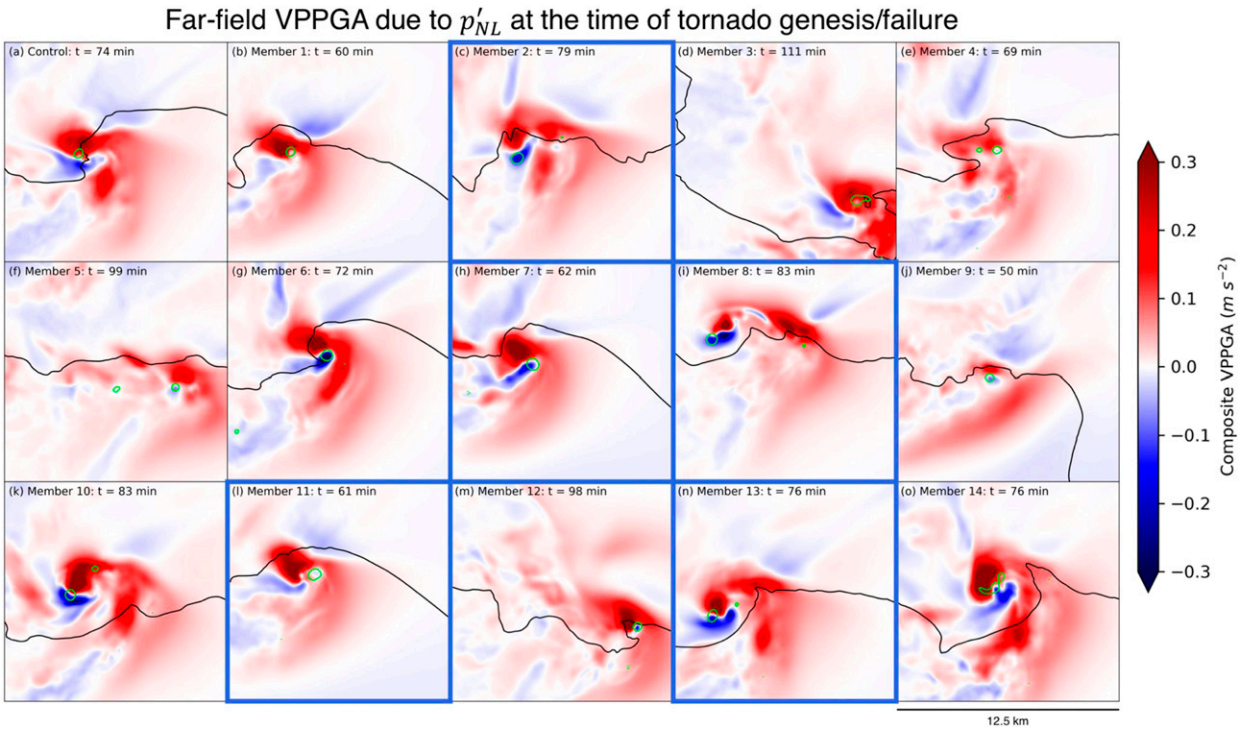

FIG. 13. As in Fig. 12, but for the 15-member far-field ensemble. The five tornadic members are outlined in blue.

details are inherently unpredictable. This is typical for cloud-model simulations of supercells up to about 2 hours (Cintineo and Stensrud 2013). Once supercell simulations reach a state in which differences in storm-scale features, like mesocyclones, arising from very small differences in the initial state become large on scales of tens of minutes and kilometers, attribution to differences in the initial condition becomes difficult. This underscores the need to use an ensemble approach to ensure representative results (Potvin et al. 2017).

An ensemble approach is also useful for examining the range of possible outcomes, in this case, with respect to storm evolution in a homogeneous environment. Anecdotal evidence is sufficient to state that some environments that seem very supportive of tornadoes may produce none, while others produce outbreaks in which nearly every storm is tornadic. Markowski and Richardson (2017) used this context to ask the question: "Do the storms on these days somehow *all* have optimal cold pool strengths and shapes (i.e., heat sink characteristics)? [...] Or is there something about some environments—yet to be discovered—that can make storms much less sensitive to the details of their cold pools?" In this case, several storms were simulated in essentially the same environments such that variations between them are attributable to storm-scale variability. The ensembles displayed different magnitudes and modes of variability, especially with respect to surface θ'_ρ (Figs. 7c, 8b, and 11) and low-level updraft characteristics (Figs. 7b and 8a). Furthermore, although both environments seemed very supportive of tornadoes based on known ingredients, one environment promoted intense surface vortex development and sustenance every time while the other did so much less frequently (e.g., Markowski and Richardson 2017). *In our case, this is due to the production of stronger low-level updrafts and intense dynamic lift as well as the restraint of cold outflow away from the developing surface vortex in the near-field ensemble.* Is it possible that in these cases the low-level updraft becomes so strong that it is able to intensify surface circulations to tornadic strength regardless of any negative buoyancy (i.e., the second question posed above)? Or is this environment capable of restraining colder outflow away from developing vortices such that weaker low-level updrafts are still able to produce tornadoes (i.e., the first question posed above)?

The results of this experiment reveal two ensembles that drastically differ in terms of sustained vortices; all members in the near-field ensemble produced tornadoes while only 33% of members in the far-field ensemble produced tornadoes (although many nontornadic members produced intense, short-lived vortices that did not last for at least 2 min). Given larger low-level directional and speed shear, the near-field wind profile is

thought to be more conducive for rapid mesocyclone development and tornado production (Thompson et al. 2007). However, both the near- and far-field soundings were derived from observations in the inflow of tornadic supercells (Parker 2014). Thus, it is interesting that the far-field ensemble only produced tornadoes 33% of the time. Why?

We generally find warmer outflow in the tornadic supercells than the nontornadic supercells. This is consistent with observed outflow temperature deficits in tornadic and nontornadic supercells (Markowski et al. 2002; Grzych et al. 2007; Hirth et al. 2008); however, the deficits in both ensembles in this study are consistent with those observed in the outflow of tornadic supercells. Storm outflow temperature is related to boundary layer relative humidity in the environment within which the storm resides (e.g., Rasmussen and Blanchard 1998; Rasmussen 2003; Markowski et al. 2003; Thompson et al. 2003; Craven and Brooks 2004; Markowski and Richardson 2009); higher boundary layer relative humidity leads to less evaporative cooling within storm-scale downdrafts, resulting in relatively warmer outflow compared to downdrafts experiencing more evaporative cooling (Kumjian 2011; French et al. 2015). Outflow temperature in the vicinity of the surface vortex is also related to the degree to which the rear-flank gust front is restrained by environmental winds (e.g., Rotunno et al. 1988; Xue 2000; Stensrud et al. 2005; Guarriello et al. 2018). This could explain why the *range* of θ'_ρ near the vortex in the near-field ensemble was much smaller than that in the far-field ensemble.

We also find significantly stronger low-level updrafts in the near-field ensemble, both in the vicinity of the developing vortex and across the entire storm for the duration of the simulations. This finding along with differences in low-level VPPGAs between the two ensembles resembles the findings of Coffer and Parker (2017) and Coffer et al. (2017) with respect to the near-field tornadic and near-field nontornadic composite VORTEX2 soundings (Parker 2014). However, there is a subtle difference in how the VPPGAs are realized. They attributed the stronger updrafts in the near-field tornadic ensemble to larger initial, low-level streamwise horizontal vorticity resulting from a critical angle closer to 90° (i.e., a larger ratio of streamwise to crosswise horizontal vorticity; Esterheld and Giuliano 2008) along parcels bound for the updraft, whereas parcels in the near-field nontornadic ensemble contained less streamwise vorticity because of larger critical angles. While the low-level streamwise vorticity is larger in the entirely tornadic near-field ensemble here, as it is in Coffer et al. (2017), the larger streamwise vorticity does not result from a critical angle closer to 90°, but rather larger vertical wind shear and storm-relative winds[6] (Fig. 14), resulting from storm-environment modifications (Parker 2014, Wade et al. 2018).

Obviously, the thresholds used to define a ''tornado'' in these simulations are arbitrary. However, differences in ''tornado'' production between the ensembles are largely insensitive to variations in all of these thresholds except for the time criteria. If the time criteria (vortex lifetime ≥ 2 min) is neglected, 12 of 15 far-field members produced a ''tornado''; these intense, short-lived vortices may represent observed, short-lived tornadoes. All ''tornadoes'' in the near-field members, however, last around 15 + minutes. This shows that even if the intense, short-lived vortices in the far-field ensemble are interpreted as tornadoes, significant differences in vortex production exist between the two ensembles, namely in the longevity of the intense surface vortices.

Along these lines, in a separate suite of seven far-field ensemble members emulating the model configuration of Coffer et al. (2017), using 100 m horizontal grid spacing in the inner domain, an updated version of the NSSL microphysics scheme included in release r19.8 of CM1, and an adaptive time step (with a large time step of approximately 1 s during the key time period), *all seven members produce tornadoes* that meet the definition outlined in section 2, including many that are as intense as vortices in the near-field ensemble. Further sensitivity tests showed that the shorter time step used herein compared to the adaptive time step in Coffer et al. (2017) possibly leads to increased implicit diffusion within the fifth-order advection scheme and weaker magnitude vortices. In addition to the storm-scale details discussed above, this may explain why vortices in the far-field ensemble do not consistently meet the time criteria outlined in section 2. While the differences between the near- and far-field ensembles in section 3 are robust for the given model configuration (i.e., the far-field ensemble has weaker, shorter-lived vortices compared to the near-field ensemble), these sensitivity tests provide further evidence of the arbitrary nature of ''tornado'' thresholds and the sensitivity of tornadogenesis to seemingly minor model configuration differences in this idealized framework.

Using the near- and far-field tornadic VORTEX2 environments in this study allowed us to investigate the impact of these storm-environment modifications (e.g., Nowotarski and Markowski 2016; Wade et al. 2018) on simulated supercell evolution and potential impacts on the volatility of tornadogenesis in each ensemble. The ensemble initialized in the far-field, tornadic environment

[6] This is consistent with analyses of tornadic and nontornadic proximity soundings in Coniglio and Parker (2020).

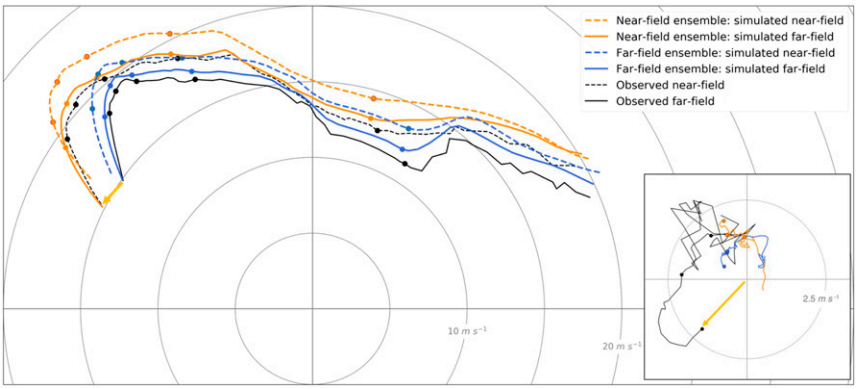

FIG. 14. Observed (black) and simulated (orange and blue) hodographs in the near- (dashed) and far-field (solid) environments. The observed hodographs (black) are the composite VORTEX2 near- and far-inflow hodographs. These are identical to those plotted in Fig. 2 of this study and in Fig. 12 of Parker (2014). Two composite hodographs extracted from the far-field ensemble are plotted in blue, and two extracted from the near-field ensemble are plotted in orange. Each of these four hodographs is a composite of 15 hodographs at either the "near-field" (40 km due southeast of the surface vortex) or "far-field" (80 km due southeast of the surface vortex) at the time of tornado genesis or failure for each ensemble member within either ensemble (near-field or far-field). Filled markers indicate heights of 100, 250, 500, 1000, and 3000 m AGL. The hodographs are plotted from 10 to 6000 m AGL and are storm-relative (i.e., storm motion is at the origin). The inset shows the difference between the near-field and far-field wind components for each case (observations, far-field ensemble, or near-field ensemble) plotted in hodograph-space. The yellow arrow indicates how this difference is plotted for the 10 m AGL winds in the composite VORTEX2 hodographs (black lines). Filled markers in this inset indicate heights of 10, 500, and 1000 m AGL.

in this study produced fewer tornadoes than the ensemble initialized in the near-field, nontornadic environment in Coffer et al. (2017). In addition to the fact that the far-field ensemble produced fewer tornadoes than the near-field ensemble, this comparison suggests that *storm-environment feedbacks can create a local environment more supportive of tornado potential.*

So, did the near-field environment in the simulations evolve in a similar manner? Fig. 14 shows that storm-environment modifications to the wind profile are indeed captured in these ensembles. Simulated modifications are similar to those depicted in the near- and far-field composite environments, except in the lowest 1 km AGL. In this layer, modification in the composite near-field resulted in backing and strengthening winds, whereas the simulated modifications resulted in mostly changes in wind speed, not direction. It is not clear why the simulated near-field low-level winds do not back, but it is noteworthy that Wade et al. (2018), in a comparison of near-simultaneous near- and far-field supercell soundings also did not show backing in the near-field winds, only an increase in speed. Therefore, sufficient observational uncertainty still exists on how storms truly modify their environments to know how well CM1 represents these processes.

This study also featured EOF analysis at the time of tornado genesis or failure. To the authors' knowledge, this type of analysis has not previously been performed on high-resolution model output of supercells. The leading modes of variability of ζ, θ'_ρ, and wind direction revealed important modes of storm-scale variability (Figs. 10 and 11). These regions are associated with physical characteristics of the storm, including the locations of storm-generated boundaries and environmental inflow. In particular, the leading EOFs in both ensembles revealed boundaries extending northward from the vortex into the core of the storm. This boundary was more prominent in the near-field ensemble with a westward gradient in variability of ζ, θ'_ρ, and wind direction (although each of these gradients were not collocated) along with a broad cyclonic wind shift. This is consistent with the presence of a vorticity river or streamwise vorticity current emanating from the core of the supercell and extending southward toward the vortex. These boundaries have been recently identified in multiple supercell simulations and, in some cases, linked with tornado potential. Some preliminary observational studies have showed the possible existence of a vorticity river or SVC in real supercells (e.g., Murdzek et al. 2018; Schueth and Weiss 2018). In both ensembles in this study, especially the near-field ensemble, *this boundary was consistently manifested in near-surface model output and demarcated regions of greater and lesser storm-scale variability in the EOF analyses.*

5. Summary

This study addresses the following questions:

1) What patterns of variability in storm characteristics and tornado potential exist between storms forming in essentially the same environment?
2) Is the volatility of tornadogenesis different in the near- and far-field VORTEX2 environments?
3) If so, what drives differences in the volatility of tornadogenesis in these environments?

To address these questions, two high-resolution ensembles of simulations were performed using CM1. A horizontal grid spacing of 125 m was sufficient to resolve supercellular low-level mesocyclones and tornado-like vortices. The two 15-member ensembles were created using the near- and far-field tornadic composite environments from VORTEX2 (Parker 2014) and applying small perturbations—within observational error—to the base-state hodographs.

Each member in both ensembles produced a right-moving supercell. Tornado genesis and failure criteria were used to establish the time of these events in each member. Based on the thresholds used, all of the near-field members produced a tornado and five of the far-field members produced a tornado. Many of the far-field members produced intense surface vortices rivaling tornado production but were not capable of sustaining them for at least 2 min. Spatial and temporal composites as well as EOF analyses were created to assess storm-scale variability and features related to the volatility of tornadogenesis in both environments. Based on the results, we present the following conclusions.

- The range of possible storms, at least in terms of tornado production, differs in different environments. In this case, the volatility of tornadogenesis in the near-field ensemble was much smaller than in the far-field ensemble.
- Larger storm-scale variability exists in the far-field ensemble than in the near-field ensemble. Compared to the near-field ensemble, increased variance in θ'_ρ and surface wind direction were evident primarily to the northeast of the surface vortex, upstream of the low-level mesocyclone.
- The near-field ensemble contained stronger low-level VPPGAs due to p'_{NL} and warmer outflow in the vicinity of the developing vortex. This may be linked to differences in the volatility of tornadogenesis between the two ensembles.
- A storm-scale boundary to the north of the vortex was evident in the near-field ensemble and was not as clear in the far-field ensemble. In the near-field ensemble, increased variance in θ'_ρ and surface wind directions were present within storm outflow to the west of the boundary and decreased variance was present in storm-cooled inflow air to the east. This is consistent with the location of some boundaries noted in recent high-resolution supercell simulations, including the streamwise vorticity current, vorticity river, and left-flank convergence boundary.

Overall, these findings shed light on the variety of storms that are possible within a given environment with observational error in vertical wind profiles, how those storms vary in terms of storm-scale evolution, and ultimately how that impacts tornado potential in those environments. A critical assumption in this study is that the differences between the near- and far-field ensembles and conclusions derived from them are solely related to the effects of storm-environment modification. It is possible that environmental heterogeneities were present in the VORTEX2 cases that also modified the local environment, resulting in one with enhanced tornado potential. Future work should focus on the representativeness of simulated storm-environment feedbacks (in both research and operational models) and pre-existing mesoscale variability using observed soundings in idealized experiments. Finally, ongoing studies using these ensembles focus on the physical processes influencing the volatility of tornadogenesis, including differences in low-level updraft strength and near-surface characteristics upstream of the mesocyclone.

Acknowledgments. The authors thank Matt Parker for his insightful discussions on this topic, as well as Martin Satrio and Sean Waugh. We also thank George Bryan for his support of CM1 and Ryan Hastings for providing the pressure decomposition code. We thank the participants of the VORTEX2 field program for collecting the data used in this study. Last, we thank the constructive comments provided by three anonymous reviewers that greatly improved the quality of this paper. This work was supported by an NSF Graduate Research Fellowship (105411900) and the NOAA/Office of Oceanic and Atmospheric Research under NOAA–University of Oklahoma Cooperative Agreement NA11OAR4320072, U.S. Department of Commerce.

REFERENCES

Barnes, S. L., 1978: Oklahoma thunderstorms on 29–30 April 1970. Part I: Morphology of a tornadic storm. *Mon. Wea. Rev.*, **106**, 673–684, https://doi.org/10.1175/1520-0493(1978)106<0673:OTOAPI>2.0.CO;2.

Beck, J., and C. Weiss, 2013: An assessment of low-level baroclinity and vorticity within a simulated supercell. *Mon. Wea. Rev.*, **141**, 649–669, https://doi.org/10.1175/MWR-D-11-00115.1.

Blumberg, W. G., K. T. Halbert, T. A. Supinie, P. T. Marsh, R. L. Thompson, and J. A. Hart, 2017: SHARPpy: An open-source sounding analysis toolkit for the atmospheric sciences. *Bull. Amer. Meteor. Soc.*, **98**, 1625–1636, https://doi.org/10.1175/BAMS-D-15-00309.1.

Bretherton, C. S., C. Smith, and J. M. Wallace, 1992: An intercomparison of methods for finding coupled patterns in climate data. *J. Climate*, **5**, 541–560, https://doi.org/10.1175/1520-0442(1992)005<0541:AIOMFF>2.0.CO;2.

Brown, M., and C. J. Nowotarski, 2019: The influence of lifting condensation level on low-level outflow and rotation in simulated supercell thunderstorms. *J. Atmos. Sci.*, **76**, 1349–1372, https://doi.org/10.1175/JAS-D-18-0216.1.

Bryan, G. H., and J. M. Fritsch, 2002: A benchmark simulation for moist nonhydrostatic numerical models. *Mon. Wea. Rev.*, **130**, 2917–2928, https://doi.org/10.1175/1520-0493(2002)130<2917:ABSFMN>2.0.CO;2.

Cintineo, R. M., and D. J. Stensrud, 2013: On the predictability of supercell thunderstorm evolution. *J. Atmos. Sci.*, **70**, 1993–2011, https://doi.org/10.1175/JAS-D-12-0166.1.

Coffer, B. E., and M. D. Parker, 2015: Impacts of increasing low-level shear on supercells during the early evening transition. *Mon. Wea. Rev.*, **143**, 1945–1969, https://doi.org/10.1175/MWR-D-14-00328.1.

——, and ——, 2017: Simulated supercells in nontornadic and tornadic VORTEX2 environments. *Mon. Wea. Rev.*, **145**, 149–180, https://doi.org/10.1175/MWR-D-16-0226.1.

——, and ——, 2018: Is there a ''tipping point'' between simulated nontornadic and tornadic supercells in VORTEX2 environments? *Mon. Wea. Rev.*, **146**, 2667–2693, https://doi.org/10.1175/MWR-D-18-0050.1.

——, ——, J. M. Dahl, L. J. Wicker, and A. J. Clark, 2017: Volatility of tornadogenesis: An ensemble of simulated nontornadic and tornadic supercells in VORTEX2 environments. *Mon. Wea. Rev.*, **145**, 4605–4625, https://doi.org/10.1175/MWR-D-17-0152.1.

——, ——, R. L. Thompson, B. T. Smith, and R. E. Jewell, 2019: Using near-ground storm relative helicity in supercell tornado forecasting. *Wea. Forecasting*, **34**, 1417–1435, https://doi.org/10.1175/WAF-D-19-0115.1.

Coniglio, M. C., and M. D. Parker, 2020: Insights into supercells and their environments from three decades of targeted radiosonde observations. *Mon. Wea. Rev.*, https://doi.org/10.1175/MWR-D-20-0105.1, in press.

Craven, J. P., and H. E. Brooks, 2004: Baseline climatology of sounding derived parameters associated with deep, moist convection. *Natl. Wea. Dig.*, **28**, 13–24.

Dahl, J. M., 2017: Tilting of horizontal shear vorticity and the development of updraft rotation in supercell thunderstorms. *J. Atmos. Sci.*, **74**, 2997–3020, https://doi.org/10.1175/JAS-D-17-0091.1.

——, M. D. Parker, and L. J. Wicker, 2014: Imported and storm-generated near-ground vertical vorticity in a simulated supercell. *J. Atmos. Sci.*, **71**, 3027–3051, https://doi.org/10.1175/JAS-D-13-0123.1.

Davies-Jones, R. P., 1982a: A new look at the vorticity equation with application to tornadogenesis. Preprints, *12th Conf. on Severe Local Storms*, San Antonio, TX, Amer. Meteor. Soc., 249–252.

——, 1982b: Observational and theoretical aspects of tornadogenesis. *Intense Atmospheric Vortices*, L. Bengtsson and J. Lighthill, Eds., Springer-Verlag, 175–189.

——, 1984: Streamwise vorticity: The origin of updraft rotation in supercell storms. *J. Atmos. Sci.*, **41**, 2991–3006, https://doi.org/10.1175/1520-0469(1984)041<2991:SVTOOU>2.0.CO;2.

——, 2015: A review of supercell and tornado dynamics. *Atmos. Res.*, **158–159**, 274–291, https://doi.org/10.1016/j.atmosres.2014.04.007.

——, and H. E. Brooks, 1993: Mesocyclogenesis from a theoretical perspective. *The Tornado: Its Structure, Dynamics, Prediction, and Hazards*, C. Church et al., Eds., Amer. Geophys. Union, 105–114.

Dawson, D. T., II, L. J. Wicker, E. R. Mansell, and R. L. Tanamachi, 2012: Impact of the environmental low-level wind profile on ensemble forecasts of the 4 May 2007 Greensburg, Kansas, tornadic storm and associated mesocyclones. *Mon. Wea. Rev.*, **140**, 696–716, https://doi.org/10.1175/MWR-D-11-00008.1.

Doswell, C. A., III, and D. W. Burgess, 1993: Tornadoes and tornadic storms: A review of conceptual models. *The Tornado: Its Structure, Dynamics, Hazards, and Prediction*, *Geophys. Monogr.*, Vol. 79, Amer. Geophys. Union, 161–172.

Esterheld, J. M., and D. J. Giuliano, 2008: Discriminating between tornadic and non-tornadic supercells: A new hodograph technique. *Electron. J. Severe Storms Meteor.*, **3** (2), http://www.ejssm.org/ojs/index.php/ejssm/issue/view/13.

French, M. M., D. W. Burgess, E. R. Mansell, and L. J. Wicker, 2015: Bulk hook echo raindrop sizes retrieved using mobile, polarimetric Doppler radar observations. *J. Appl. Meteor. Climatol.*, **54**, 423–450, https://doi.org/10.1175/JAMC-D-14-0171.1.

Glickman, T., Ed., 2000: *Glossary of Meteorology*. 2nd ed. Amer. Meteor. Soc., 855 pp., http://glossary.ametsoc.org/.

Grzych, M. L., B. D. Lee, and C. A. Finley, 2007: Thermodynamic analysis of supercell rear-flank downdrafts from project ANSWERS. *Mon. Wea. Rev.*, **135**, 240–246, https://doi.org/10.1175/MWR3288.1.

Guarriello, F., C. J. Nowotarski, and C. C. Epifanio, 2018: Effects of the low-level wind profile on outflow position and near-surface vertical vorticity in simulated supercell thunderstorms. *J. Atmos. Sci.*, **75**, 731–753, https://doi.org/10.1175/JAS-D-17-0174.1.

Hastings, R., and Y. Richardson, 2016: Long-term morphological changes in simulated supercells following mergers with nascent supercells in directionally varying shear. *Mon. Wea. Rev.*, **144**, 471–499, https://doi.org/10.1175/MWR-D-15-0193.1.

Hirth, B. D., J. L. Schroeder, and C. C. Weiss, 2008: Surface analysis of the rear-flank downdraft outflow in two tornadic supercells. *Mon. Wea. Rev.*, **136**, 2344–2363, https://doi.org/10.1175/2007MWR2285.1.

Klees, A. M., Y. P. Richardson, P. M. Markowski, C. Weiss, J. M. Wurman, and K. K. Kosiba, 2016: Comparison of the tornadic and nontornadic supercells intercepted by VORTEX2 on 10 June 2010. *Mon. Wea. Rev.*, **144**, 3201–3231, https://doi.org/10.1175/MWR-D-15-0345.1.

Klemp, J. B., and R. Rotunno, 1983: A study of the tornadic region within a supercell thunderstorm. *J. Atmos. Sci.*, **40**, 359–377, https://doi.org/10.1175/1520-0469(1983)040<0359:ASOTTR>2.0.CO;2.

Kumjian, M. R., 2011: Precipitation properties of supercell hook echoes. *Electron. J. Severe Storms Meteor.*, 6 (5), http://ejssm.org/ojs/index.php/ejssm/article/viewArticle/93.

Lilly, D. K., 1982: The development and maintenance of rotation in convective storms. *Intense Atmospheric Vortices*, L.Bengtsson and J. Lighthill, Eds., Springer-Verlag, 149–160.

Lorenz, E. N., 1956: Empirical orthogonal functions and statistical weather prediction. Statistical Forecasting Project Sci.

Rep. 1, MIT, 52 pp., https://eapsweb.mit.edu/sites/default/files/Empirical_Orthogonal_Functions_1956.pdf.

Mansell, E. R., 2010: On sedimentation and advection in multi-moment bulk microphysics. *J. Atmos. Sci.*, **67**, 3084–3094, https://doi.org/10.1175/2010JAS3341.1.

——, C. L. Ziegler, and E. C. Bruning, 2010: Simulated electrification of a small thunderstorm with two-moment bulk microphysics. *J. Atmos. Sci.*, **67**, 171–194, https://doi.org/10.1175/2009JAS2965.1.

Markowski, P. M., 2008: A comparison of the midlevel kinematic characteristics of a pair of supercell thunderstorms observed by airborne Doppler radar. *Atmos. Res.*, **88**, 314–322, https://doi.org/10.1016/j.atmosres.2007.11.026.

——, and Y. P. Richardson, 2009: Tornadogenesis: Our current understanding, forecasting considerations, and questions to guide future research. *Atmos. Res.*, **93**, 3–10, https://doi.org/10.1016/j.atmosres.2008.09.015.

——, and ——, 2010: *Mesoscale Meteorology in Midlatitudes*. Wiley-Blackwell, 372 pp.

——, and ——, 2014: The influence of environmental low-level shear and cold pools on tornadogenesis: Insights from idealized simulations. *J. Atmos. Sci.*, **71**, 243–275, https://doi.org/10.1175/JAS-D-13-0159.1.

——, and G. H. Bryan, 2016: LES of laminar flow in the PBL: A potential problem for convective storm simulations. *Mon. Wea. Rev.*, **144**, 1841–1850, https://doi.org/10.1175/MWR-D-15-0439.1.

——, and Y. P. Richardson, 2017: Large sensitivity of near-surface vertical vorticity development to heat sink location in idealized simulations of supercell-like storms. *J. Atmos. Sci.*, **74**, 1095–1104, https://doi.org/10.1175/JAS-D-16-0372.1.

——, J. M. Straka, E. N. Rasmussen, and D. O. Blanchard, 1998: Variability of storm-relative helicity during VORTEX. *Mon. Wea. Rev.*, **126**, 2959–2971, https://doi.org/10.1175/1520-0493(1998)126<2959:VOSRHD>2.0.CO;2.

——, ——, and ——, 2002: Direct surface thermodynamic observations within the rear-flank downdrafts of nontornadic and tornadic supercells. *Mon. Wea. Rev.*, **130**, 1692–1721, https://doi.org/10.1175/1520-0493(2002)130<1692:DSTOWT>2.0.CO;2.

——, ——, and ——, 2003: Tornadogenesis resulting from the transport of circulation by a downdraft: Idealized numerical simulations. *J. Atmos. Sci.*, **60**, 795–823, https://doi.org/10.1175/1520-0469(2003)060<0795:TRFTTO>2.0.CO;2.

——, Y. P. Richardson, M. Majcen, J. Marquis, and J. Wurman, 2011: Characteristics of the wind field in three nontornadic low-level mesocyclones observed by the Doppler on Wheels radars. *Electron. J. Severe Storms Meteor.*, **6** (3), https://www.ejssm.org/ojs/index.php/ejssm/article/viewArticle/75.

——, and Coauthors, 2012a: The pretornadic phase of the Goshen County, Wyoming, supercell of 5 June 2009 intercepted by VORTEX2. Part I: Evolution of kinematic and surface thermodynamic fields. *Mon. Wea. Rev.*, **140**, 2887–2915, https://doi.org/10.1175/MWR-D-11-00336.1.

——, and Coauthors, 2012b: The pretornadic phase of the Goshen County, Wyoming, supercell of 5 June 2009 intercepted by VORTEX2. Part II: Intensification of low-level rotation. *Mon. Wea. Rev.*, **140**, 2916–2938, https://doi.org/10.1175/MWR-D-11-00337.1.

——, Y. Richardson, and G. Bryan, 2014: The origins of vortex sheets in a simulated supercell thunderstorm. *Mon. Wea. Rev.*, **142**, 3944–3954, https://doi.org/10.1175/MWR-D-14-00162.1.

——, T. Hatlee, and Y. Richardson, 2018: Tornadogenesis in the 12 May 2010 supercell thunderstorm intercepted by VORTEX2 near Clinton, Oklahoma. *Mon. Wea. Rev.*, **146**, 3623–3650, https://doi.org/10.1175/MWR-D-18-0196.1.

Mercer, A. E., C. E. Shafer, C. A. Doswell, L. M. Leslie, and M. B. Richman, 2012: Synoptic composites of tornadic and nontornadic outbreaks. *Mon. Wea. Rev.*, **140**, 2590–2608, https://doi.org/10.1175/MWR-D-12-00029.1.

Murdzek, S. S., E. N. Rasmussen, and M. D. Flournoy, 2018: Mobile mesonet observations near vorticity rivers in supercells. *29th Conf. on Severe Local Storms*, Stowe, VT, Amer. Meteor. Soc., P96, https://ams.confex.com/ams/29SLS/webprogram/Paper348792.html.

Naylor, J., and M. S. Gilmore, 2012: Convective initiation in an idealized cloud model using an updraft nudging technique. *Mon. Wea. Rev.*, **140**, 3699–3705, https://doi.org/10.1175/MWR-D-12-00163.1.

Nowotarski, C. J., and P. M. Markowski, 2016: Modifications to the near-storm environment induced by simulated supercell thunderstorms. *Mon. Wea. Rev.*, **144**, 273–293, https://doi.org/10.1175/MWR-D-15-0247.1.

Orf, L., R. Wilhelmson, B. Lee, C. Finley, and A. Houston, 2017: Evolution of a long-track violent tornado within a simulated supercell. *Bull. Amer. Meteor. Soc.*, **98**, 45–68, https://doi.org/10.1175/BAMS-D-15-00073.1.

Parker, M. D., 2014: Composite VORTEX2 supercell environments from near-storm soundings. *Mon. Wea. Rev.*, **142**, 508–529, https://doi.org/10.1175/MWR-D-13-00167.1.

——, and J. M. Dahl, 2015: Production of near-surface vertical vorticity by idealized downdrafts. *Mon. Wea. Rev.*, **143**, 2795–2816, https://doi.org/10.1175/MWR-D-14-00310.1.

Potvin, C. K., E. M. Murillo, M. L. Flora, and D. M. Wheatley, 2017: Sensitivity of supercell simulations to initial-condition resolution. *J. Atmos. Sci.*, **74**, 5–26, https://doi.org/10.1175/JAS-D-16-0098.1.

Rasmussen, E. N., 2003: Refined supercell and tornado forecast parameters. *Wea. Forecasting*, **18**, 530–535, https://doi.org/10.1175/1520-0434(2003)18<530:RSATFP>2.0.CO;2.

——, and D. O. Blanchard, 1998: A baseline climatology of sounding-derived supercell and tornado forecast parameters. *Wea. Forecasting*, **13**, 1148–1164, https://doi.org/10.1175/1520-0434(1998)013<1148:ABCOSD>2.0.CO;2.

——, J. M. Straka, M. S. Gilmore, and R. Davies-Jones, 2006: A preliminary survey of rear-flank descending reflectivity cores in supercell storms. *Wea. Forecasting*, **21**, 923–938, https://doi.org/10.1175/WAF962.1.

Richman, M. B., 1980: Map typing associated with potential urban enhanced precipitation. M. S. thesis, Department of Atmospheric Sciences, University of Illinois at Urbana–Champaign, 123 pp.

Roberts, B., M. Xue, A. D. Schenkman, and D. T. Dawson, 2016: The role of surface drag in tornadogenesis within an idealized supercell simulation. *J. Atmos. Sci.*, **73**, 3371–3395, https://doi.org/10.1175/JAS-D-15-0332.1.

Rotunno, R., 1981: On the evolution of thunderstorm rotation. *Mon. Wea. Rev.*, **109**, 577–586, https://doi.org/10.1175/1520-0493(1981)109<0577:OTEOTR>2.0.CO;2.

——, and J. Klemp, 1985: On the rotation and propagation of simulated supercell thunderstorms. *J. Atmos. Sci.*, **42**, 271–292, https://doi.org/10.1175/1520-0469(1985)042<0271:OTRAPO>2.0.CO;2.

——, ——, and M. L. Weisman, 1988: A theory for strong, long-lived squall lines. *J. Atmos. Sci.*, **45**, 463–485, https://doi.org/10.1175/1520-0469(1988)045<0463:ATFSLL>2.0.CO;2.

Schaefer, J., and C. A. Doswell III, 1984: Empirical orthogonal function expansion applied to progressive tornado outbreaks.

J. Meteor. Soc. Japan, **62**, 929–936, https://doi.org/10.2151/jmsj1965.62.6_929.

Schenkman, A. D., M. Xue, and M. Hu, 2014: Tornadogenesis in a high-resolution simulation of the 8 May 2003 Oklahoma City supercell. *J. Atmos. Sci.*, **71**, 130–154, https://doi.org/10.1175/JAS-D-13-073.1.

Schueth, A., and C. C. Weiss, 2018: Comparing observations and simulations of the streamwise vorticity current in a tornadic supercell storm. *29th Conf. on Severe Local Storms*, Stowe, VT, Amer. Meteor. Soc., 3B.6, https://ams.confex.com/ams/29SLS/webprogram/Paper348686.html.

Stensrud, D. J., M. C. Coniglio, R. Davies-Jones, and J. Evans, 2005: Comments on "'A theory for strong long-lived squall lines' revisited." *J. Atmos. Sci.*, **62**, 2989–2996, https://doi.org/10.1175/JAS3514.1.

Thompson, R. L., and R. Edwards, 2000: A comparison of Rapid Update Cycle 2 (RUC-2) model soundings with observed soundings in supercell environments. Preprints, *20th Conf. on Severe Local Storms*, Orlando, FL, Amer. Meteor. Soc., 551–554.

——, ——, J. A. Hart, K. L. Elmore, and P. Markowski, 2003: Close proximity soundings within supercell environments obtained from the Rapid Update Cycle. *Wea. Forecasting*, **18**, 1243–1261, https://doi.org/10.1175/1520-0434(2003)018<1243:CPSWSE>2.0.CO;2.

——, C. M. Mead, and R. Edwards, 2007: Effective storm-relative helicity and bulk shear in supercell thunderstorm environments. *Wea. Forecasting*, **22**, 102–115, https://doi.org/10.1175/WAF969.1.

Trapp, R. J., 1999: Observations of nontornadic low-level mesocyclones and attendant tornadogenesis failure during VORTEX. *Mon. Wea. Rev.*, **127**, 1693–1705, https://doi.org/10.1175/1520-0493(1999)127<1693:OONLLM>2.0.CO;2.

Wade, A. R., M. C. Coniglio, and C. L. Ziegler, 2018: Comparison of near-and far-field supercell inflow environments using radiosonde observations. *Mon. Wea. Rev.*, **146**, 2403–2415, https://doi.org/10.1175/MWR-D-17-0276.1.

Wakimoto, R. M., and H. Cai, 2000: Analysis of a nontornadic storm during VORTEX 95. *Mon. Wea. Rev.*, **128**, 565–592, https://doi.org/10.1175/1520-0493(2000)128<0565:AOANSD>2.0.CO;2.

Wicker, L. J., and R. B. Wilhelmson, 1995: Simulation and analysis of tornado development and decay within a three-dimensional supercell thunderstorm. *J. Atmos. Sci.*, **52**, 2675–2703, https://doi.org/10.1175/1520-0469(1995)052<2675:SAAOTD>2.0.CO;2.

Wurman, J., D. Dowell, Y. Richardson, P. Markowski, E. Rasmussen, D. Burgess, L. Wicker, and H. Bluestein, 2012: The second Verification of the Origins of Rotation in Tornadoes Experiment 2: VORTEX2. *Bull. Amer. Meteor. Soc.*, **93**, 1147–1170, https://doi.org/10.1175/BAMS-D-11-00010.1.

Xue, M., 2000: Density currents in two-layer shear flows. *Quart. J. Roy. Meteor. Soc.*, **126**, 1301–1320, https://doi.org/10.1002/qj.49712656506.

Ziegler, C. L., 1985: Retrieval of thermal and microphysical variables in observed convective storms. Part I: Model development and preliminary testing. *J. Atmos. Sci.*, **42**, 1487–1509, https://doi.org/10.1175/1520-0469(1985)042<1487:ROTAMV>2.0.CO;2.